ARSENIC-BEARING SERPENTINE-GROUP MINERALS: MINERAL SYNTHESIS WITH INSIGHTS FOR THE ARSENIC CYCLE

P. C. Ryan[1,2]* , F.J. Huertas[2], L. N. Pincus[3], and W. Painter[1]

[1]Department of Geology, Middlebury College, 276 Bicentennial Way, Middlebury, VT 05763, USA
[2]Instituto Andaluz de Ciencias de la Tierra, Avda. Palmeras 4, Armilla, 18100 Granada, Spain
[3]School of Forestry and Environmental Studies, Yale University, 195 Prospect Street, New Haven, CT 06511, USA

Abstract—When present at elevated levels in drinking water, arsenic is toxic, and magnesian clays are gaining recognition as a source of elevated arsenic in groundwater. In the crust and upper mantle of Earth, arsenic incorporation into clay minerals is influenced by geochemical conditions associated with hydrothermal fluids and metamorphic processes (e.g. serpentinization), meaning that As is a useful tracer of fluid-flow in the deep Earth. To improve understanding of arsenic speciation in groundwater, sediments, soils, and hydrothermal-metamorphic systems, the present study examined arsenic incorporation into magnesian clays by synthesis of serpentine minerals (200°C, 10 d) with varied concentrations of Si, Al, As^{5+}, and As^{3+}. The synthesis experiments produced two distinct crystal types, tubular and platy serpentines, each with 10–15% randomly interstratified talc layers. X-ray absorption spectroscopy indicated that As^{5+} and As^{3+} occurred in the tetrahedral sheet. Single-crystal analysis revealed that tubular crystals contained up to 1 wt.% arsenic $[Mg_{2.8}(Si_{1.8}As_{0.2})O_5(OH)_4]$ (mean 0.2 wt.% As). The mean composition of platy, high-Al crystals is $(Mg_{1.8}Al_{0.7})(Si_{2.0})O_5(OH)_4$, and that of platy, medium-Al crystals with As^{3+} is $(Mg_{2.07}Al_{0.52})$ $(Si_{1.97}As^{3+}_{0.03})O_5(OH)_4$. Charge, geometry, and radius of tetrahedral AsO_4^{3-} oxyanions are similar to tetrahedral SiO_4^{4-}, and this facilitates fixation of As^{5+} into the tetrahedral sheet of clay minerals. The geometry and size of the larger As^{3+} in tetrahedral sites (as a pyramidal AsO_3^{3-} oxyanion) may limit incorporation relative to As^{5+}. Arsenic-bearing Mg clays crystallize in alkaline environments where AsO_4^{3-} or AsO_3^{3-} are the dominant As species and where high pH accompanies crystallization of serpentine, talc, chlorite, or Mg-smectite. The presence of tetrahedral As in these clays raises the possibility of tetrahedral As in other Mg clays (e.g. sepiolite or kerolite) as well.

Keywords—Aquifer · Arsenic · Hydrothermal · Mineral synthesis · Serpentine · Tetrahedral

INTRODUCTION

The behavior of arsenic in rocks, sediments, and soils is controlled strongly by its speciation in minerals and amorphous solids, and this in turn has important implications for understanding arsenic fate and transport in systems ranging from low temperature (e.g. aquifers and soils) to medium and high temperature (e.g. hydrothermal, igneous, and metamorphic systems). In groundwater, arsenic is a toxic element that adversely affects the health of at least tens of millions of people globally (Bhattacharya et al. 2007; Navas-Acien et al. 2010; Shi et al. 2015), so improved understanding of arsenic speciation is crucial to predicting uptake and release in environmental systems. The presence of As in magnesian clays is a source of elevated As in aquifers (Guillot & Charlet 2007; Ryan et al. 2011; Masuda et al. 2012), and has also proven useful for tracing fluid flow associated with subduction and metamorphism (Hattori et al. 2005; Deschamps et al. 2010). To date, however, no study has used mineral synthesis to examine systematically factors controlling the crystallochemical occurrence of As in the mineralogical structure of magnesian clays, thus providing the impetus for this study.

The oxidation states of arsenic range from As^{3-} to As^{5+}, where the low oxidation states (e.g. As^{3-}, As^0) tend to occur in sulfides and arsenides and the higher oxidations states (e.g. As^{3+}, As^{5+}) in oxides, hydroxides, and silicates. The occurrence of As in sulfides (e.g. pyrite and arsenopyrite), arsenides (e.g. skutterudite, löllingite), and in iron (oxyhydr)oxides such as goethite and magnetite (Smedley & Kinniburgh 2002; Hattori et al. 2005) is well known. The occurrence of As in silicates is less well known, but X-ray absorption spectroscopy (XAS) indicates that As occurs in tetrahedral sites (Hattori et al. 2005; Charnock et al. 2007; Niu, 2011; Masuda et al. 2012; Masuda, 2018), where As^{5+} or As^{3+} may substitute for Si^{4+}. Paired substitution of As^{5+} and As^{3+} may satisfy charge balance, and so too may paired substitution of As^{5+} and Al^{3+}. All known occurrences of As-bearing phyllosilicates are associated with alkaline fluids and serpentinization (Hattori et al. 2005; Guillot & Charlet 2007; Deschamps et al. 2010; Ryan et al. 2011) or hydrothermal mineral precipitation (Pascua et al. 2005); from these origins, As-bearing phyllosilicates may be

Electronic supplementary material The online version of this article (https://doi.org/10.1007/s42860-019-00040-1) contains supplementary material, which is available to authorized users.

A note on terminology of arsenic species: to avoid confusion with the often imprecise terms arsenate and arsenite, this article uses "As^{5+}" and "As^{3+}" as much as possible. As used herein, these are effectively equivalent to As(V) and As(III).

* E-mail address of corresponding author: pryan@middlebury.edu

eroded and deposited in sediments, where they contribute to high arsenic in groundwater (Guillot & Charlet 2007; Ryan et al. 2011; Masuda et al. 2012).

Documented arsenic occurrences in Mg phyllosilicates include antigorite, chlorite, smectite, and talc. Hattori et al. (2005) used X-ray absorption near-edge spectroscopy (XANES) and extended X-ray absorption fine-structure spectroscopy (XAFS) to document tetrahedral As^{5+} in antigorites that contain 6 to 275 mg kg^{-1} As in Himalayan serpentinites. Serpentinites from other orogenic belts have been recognized with >10 mg kg^{-1} As, and many with >100 mg kg^{-1} As (Deschamps et al. 2010; Ryan et al. 2011). Guillot & Charlet (2007) argued that antigorites are the primary source of As in the aquifer of the Bengal Fan. Ryan et al. (2011) and Niu (2011) determined (XAS, electron microprobe analysis [EMPA], and sequential extraction) that tetrahedral As^{3+} occurs in the silicate structure of antigorite in serpentinites from the northern Appalachians of the USA – these antigorites contain 20 to 450 mg kg^{-1} As, and weathering of antigorite appears to be a source of elevated As in groundwater. Masuda et al. (2012) used micro-X-ray-fluorescence (μ-XRF) to document As^{5+} and As^{3+} in chlorite that is attributed to the high As concentration in groundwater of the Holocene aquifer system in Bangladesh. Pascua et al. (2005) used XAS in conjunction with chemical extraction to document the presence of both As^{5+} and As^{3+} in trioctahedral Mg- smectite with 1500 to 4000 mg kg^{-1} As (~0.1 As per 4 tetrahedral sites) formed in a hydrothermal setting. Sequential chemical extraction and quantitative mineral analysis indicates that 50 to 140 mg kg^{-1} of As occurs in talc formed in the alteration halo surrounding serpentinites (Ryan et al. 2011). Tetrahedral As is not restricted to Mg-phyllosilicates as it has also been detected in tetrahedral sites in andradite garnet (Charnock et al. 2007).

Considering radii and charges of ions in silicate minerals, the occurrence of arsenic in tetrahedral sites in phyllosilicates is predictable; in terms of crystal radii (Shannon, 1976), As^{5+} (0.48 Å) is a better fit in the tetrahedral sheet than is Al^{3+} (0.53 Å) (compared to Si^{4+} at 0.40 Å). The magnitude of the charge difference between As^{5+} and Si^{4+} is equal to that of Al^{3+} for Si^{4+}. In fact, paired substitution of As^{5+} and Al^{3+} in tetrahedral sites for two Si^{4+} (As^{5+} + Al^{3+} ➔ 2 Si^{4+}) was suggested to explain the occurrence of tetrahedral As^{5+} in Himalayan antigorites (Hattori et al. 2005). The As^{3+} ion forms a pyramidal geometry in $AsO_3{}^{3-}$ that may limit compatibility in the tetrahedral sheet, but its crystal radius (0.54 Å) in tetrahedral coordination is comparable to that of Al^{3+} and is smaller than Fe^{3+} (0.63 Å), so the occurrence of tetrahedral As^{3+} in serpentine (antigorite; Niu, 2011) and potentially other phyllosilicates also should be explored.

One way to examine the potential for a mineral to incorporate trace elements is by mineral synthesis under controlled conditions. Such an approach can limit the number of variables and unknowns common to naturally occurring minerals, which is important when assessing trace-element speciation (Petit & Decarreau 1990; Iriarte et al. 2005; Bentabol et al. 2006, 2007, 2009). A prior synthesis study showed the potential of

serpentine to contain up to 3000 mg kg^{-1} As (0.02 mol As per 2 tetrahedral sites) (Lafay et al. 2016) (tetrahedral vs octahedral occupancy was not assessed). Considering synthesis of As-bearing Mg phyllosilicates, the ability to control for the absence of Fe simplifies the system, eliminating the possibility of As speciation into Fe-(oxyhydr)oxides. Synthesis also allows concentrations of Al^{3+}, As^{5+}, and As^{3+} to be adjusted, enabling analysis of controls on As incorporation. The method selected for synthesis of As-bearing serpentine group minerals uses salts of Mg, Al, Si, and As under alkaline conditions at 200°C and 10 d.

The purpose of this study was to carry out synthesis reactions to examine the potential for, and controls on, the incorporation of As^{5+} and As^{3+} into tetrahedral sites in serpentine group minerals. Data on mineral structures and composition were used to understand the incorporation of As into serpentine and the partitioning of As^{5+}, As^{3+}, and Al^{3+} relative to tetrahedral Si in structural sites – tetrahedral and octahedral – in the layered trioctahedral silicate. A testable hypothesis was that synthesized serpentines will incorporate As at levels at least comparable to – or greater than – natural serpentines. In addition, when charge, radius, and geometry of oxyanion (e.g. tetrahedral $As^{5+}O_4$ vs octahedral $As^{3+}O_3$) are considered, a preference was expected for As^{5+} over As^{3+} in tetrahedral sites in serpentine. Paired substitutions that maintain charge balance will foster greater incorporation of As than cases where vacancies are the only mechanism that could compensate for charge imbalance.

MATERIALS AND METHODS

Synthesis of Serpentine-group Minerals

Stock solutions of salts containing Mg, Si, Al, As^{5+}, and As^{3+} were prepared following the approach developed by Opiso et al. (2010) with some changes made to suit the objectives of this study and the synthesis equipment available. No Fe was used in the experiments. Sources of elements were as follows: Mg was from $Mg(NO_3)_2 \cdot 6H_2O$; Si was from $Na_2SiO_3 \cdot 5H_2O$; Al was from $Al(NO_3)_3 \cdot 9H_2O$; As^{5+} was from $Na_2HAsO_4 \cdot 7H_2O$; and As^{3+} was from $NaAsO_2$. With respect to the elements of interest, the molarities of stock solutions were 32.0 mM Mg and 22.5 mM for Si, Al, As^{5+}, and As^{3+}. The stock solutions were mixed to produce 3:2 molar ratios of Mg:Si for pure Mg-Si serpentines, and Si was adjusted downward in concert with quantities of Al, As^{5+}, and As^{3+} added to the synthesis solution (Table 1). The total volume of mixed reactants (~12 mL) was mixed with 13.3 mL of a NaHCO$_3$-NaOH buffer (0.05 M NaHCO$_3$ and 0.3 M NaOH at pH = 12) to produce a 25 mL solution with initial pH of 10.0 ± 0.1. This solution was reacted at 200°C for 10 d in 50 mL Teflon-lined Parr 4744 steel reactors at a pressure of 15 atm (Parr Instrument Co., Moline, Illinois, USA).

In order to avoid contamination, reactors were rinsed with milliQ water prior to synthesis then soaked overnight in the buffer solution. Reactors were then rinsed again with milliQ and dried, then filled with the synthesis reagents. In all, seven different compositions of serpentine were targeted (Table 1),

Table 1 Quantities of stock solutions of reagents (mL) mixed and added to Parr 4744 reactors for synthesis reactions. In each case, 13.325 mL of a pH 12 NaOH-NaHCO$_3$ buffer was added to produce a ~25 mL final volume at pH = 10. The right column shows the expected formula if resulting products are proportional to initial solution. See text for stock solution compositions

ID	Mg stock	Si stock	Al stock	As^{3+} stock	As^{5+} stock	Targeted serpentine composition
Serp1	6.0	6.0	--	--	--	$Mg_3Si_2O_5(OH)_4$
Serp2	6.0	5.6	0.2	--	0.2	$Mg_3(Si_{1.88}Al_{0.06}As^{5+}_{0.06})O_5(OH)_4$
Serp3	6.0	5.6	--	--	0.4	$Mg_{2.88}(Si_{1.88}As^{5+}_{0.12})O_5(OH)_4$
Serp4	6.0	5.6	0.4	--	--	$Mg_{2.94}Al_{0.06}(Si_{1.94}Al_{0.06})O_5(OH)_4$
Serp5	6.0	5.6	--	0.2	0.2	$Mg_3(Si_{1.88}As^{3+}_{0.06}As^{5+}_{0.06})O_5(OH)_4$
Serp6	6.0	5.6	0.2	0.2	--	$Mg_{2.94}Al_{0.06}(Si_{1.94}As^{3+}_{0.06})O_5(OH)_4$
Serp7	6.0	5.6	--	0.4	--	$Mg_3(Si_{1.88}As^{3+}_{0.12})O_5(OH)_4$

from pure Mg-Si serpentine to six different stoichiometric ratios of Mg, Si, and variably Al, As^{5+}, or As^{3+}. Suppliers of reagents were as follows: Mg(NO$_3$)$_2$·6H$_2$O, Al(NO$_3$)$_3$·9H$_2$O, and NaOH (Panreac Quimica S.A., Barcelona, Spain); Na$_2$SiO$_3$·5H$_2$O, Na$_2$HAsO$_4$·7H$_2$O, and NaAsO$_2$ (Sigma Aldrich Co., St. Louis, Missouri, USA); and NaHCO$_3$ (Merck, Darmstadt, Germany). Reactors were cooled quickly by submersing in cold water at the end of each experiment to ensure that the reactor was cool enough to open without spraying steam and synthesized product; as such, solids were separated as soon as possible from solutions by centrifugation.

The 10 d reaction produced white powders ranging in mass from 5 to 19 mg. In order to increase the amount of powder available for analysis, three replicate trials for each stoichiometric objective were carried out and powders were homogenized. To remove adsorbed Al, As, Mg, or Si, the synthesized powders were suspended in a 20 mL solution of 0.5 M CaCl$_2$ (from CaCl$_2$·2H$_2$O, Panreac Quimica S.A., Barcelona, Spain), which was ultrasonicated to disaggregate the powder. This suspension was allowed to equilibrate overnight, and solids were obtained by centrifuging at 5000 rpm (~1600 × g) for 15 min. This process was repeated again with 0.05 and 0.005 M solutions of CaCl$_2$, pouring off supernatant in each case. The resulting Ca-saturated clays were then subsequently washed three times with deionized water to remove any Ca not electrostatically attracted to mineral particles. Ca-washed powders from the three replicate trials were dried at 60°C, mixed, and ground gently to homogenize for instrumental analysis.

X-ray Diffraction (XRD)

X-ray diffraction analysis was performed on synthesized powders using a PANalytical X'Pert Pro system operating at 45 kV and 40 mA with an X'Celerator detector, CuKα radiation, a Ni filter, and 0.25° divergence slit. Sample mounts were prepared by pipetting concentrated slurries of powders (in ethyl alcohol) onto glass slides and allowing the slurry to evaporate – these mounts were scanned continuously from 5 to 70°2θ (0.4°2θ/min) in ambient air-dried and ethylene glycol-solvated conditions. *NEWMOD 2©* (Release 1.3;

https://newmod-for-clays.com/) was employed to model layer types using default parameters. The serpentine layer had a 7.3 Å d spacing and contained no Fe. The talc-like layer type was modeled with a 9.3 Å d spacing and no Fe, no interlayer cation and no interlayer water.

Transmission Electron Microscopy (TEM)

Transmission electron microscopy analyses were performed at the Centro de Instrumentación Científica (CIC) at the Universidad de Granada (Spain). All seven samples were first analyzed using a Philips CM-20 electron microscope (Almelo, The Netherlands) fitted with an ultrathin window and solid state Si(Li) detector for energy dispersive X-ray analysis (EDX; Mahwah, New Jersey, USA). The synthesized powders were suspended in pure ethyl alcohol and mounted on Cu grids, and analyses were performed at 200 kV with a 200 nm spot size. The compositions of single crystals were determined by analytical electron microscopy (TEM-AEM), where atomic proportions of Mg, Al, Si, and O were calculated from peak intensities (Kα lines) and converted into atomic concentrations using natural mineral standards (e.g. biotite, muscovite, olivine) with calibration carried out by the method of Cliff & Lorimer (1975). Arsenic was quantified using the Kα peak at 10.532 keV using theoretical basis for intensity, and the signal from the As 1.282 keV Lα peak was subtracted from the 1.253 Kα Mg peak to provide precise Mg intensity. The detection limit for As in TEM-AEM analyses of these synthesized serpentines was 0.1 wt.% or 1000 mg kg^{-1} (this is the concentration above which the As peak is distinct and ≥3 standard deviations above the mean of the background).

Three selected samples (Serp 1, Serp 4, and Serp 5) were analyzed using an FEI Titan G2 TEM (FEI, Hillsboro, Oregon, USA), with an XFEG emission gun, a spherical aberration corrector, and a high-angle annular dark-field (HAADF) detector. The synthesized powders were mounted in epoxy and cut to emphasize as many possible crystallographic orientations as possible. Analyses were performed at 300 kV with a resolution of ~0.2 nm in the high-resolution (HRTEM) mode

and ~2 nm in scanning TEM (STEM) mode (where the STEM method use an HAADF detector. Compositional analysis was performed with a Super X micro X-ray analyzer equipped with four detectors by X-ray energy dispersion (EDX). Elements were quantified by the same approach described above for the CM-20.

Inductively Coupled Plasma–Mass Spectrometry (ICPMS)

The chemical composition of synthesized powders was determined by ICPMS as follows: 10 mg of synthesized powder was dissolved in 10 mL of aqua regia (US EPA method 200.2, consisting of 2.9 mL of 50% HNO_3 and 7.1 mL of 20% HCl, trace metal grade [Sigma Aldrich Co., St. Louis, Missouri, USA], at 95^oC for 0.5 h), then diluted by pipetting 1.0 mL of this solution into 9.0 mL of 5% trace metal grade HNO_3. Then, 4.9 mL of this solution was mixed with 0.1 mL of an internal standard solution containing Sc and Ga. This 5.0 mL solution was analyzed using a Thermo iCAP Qc (Waltham, Massachusetts, USA) in KED mode at Middlebury College, calibrated using standards across the range of concentrations encountered, further calibrated by running NIST 1643f (National Institute of Standards and Testing, Gaithersburg, Maryland, USA) as an unknown, and drift corrected by monitoring intensities of Sc and Ga. Si could not be measured precisely due to problems with Si saturation, so the data reported pertain only to Mg, Al, and As, and are used as a means of assessing concentrations of those elements compared to TEM-AEM.

X-ray Absorption Near Edge Spectroscopy (XANES) and X-ray Absorption Fine Structure (XAFS)

In order to assess As oxidation state and coordination, XANES and XAFS were used to study synthesized powder Serp 5, the one that contained both As^{5+} and As^{3+} in the initial solution. The sample was placed on Kapton tape for analysis. XANES and XAFS spectra were collected at the As K-edge (11867 eV) at the Inner Shell Spectroscopy beamline (8-ID) at the National Synchrotron Light Source II at Brookhaven National Laboratory. The electron storage ring was operating at 3 GeV with a beam current of 400 mA. Spectra were acquired in fluorescence mode at room temperature using a cryogenically cooled Si (111) double crystal monochromator and a passivated, implanted, planar silicon (PIPS) detector. A germanium Z1 filter was used to decrease flux, minimizing sample degradation. Spectra were calibrated to the Au L-edge (11919 eV) using reference foils measured with each sample (Müller et al. 2010). Multiple scans were collected and averaged to improve the signal to noise ratio, and no oxidation or reduction of samples occurred during analysis. Data reduction and analysis of XANES spectra were performed using the *ATHENA* program (Ravel & Newville 2005). To determine relative percentages of As^{5+} and As^{3+} within the sample, linear combination fitting (LCF) was performed using the *ATHENA* program (Arai et al. 2001; Ravel & Newville 2005). The standards were 100 mMol solutions of $NaAsO_2$ and $Na_2HAsO_4 \cdot 7H_2O$ (Sigma Aldrich Co., St. Louis, Missouri, USA). Analysis of XAFS spectra was performed using the *ATHENA* (Newville 2001) and *Artemis* (Ravel & Newville

2005) programs. Uncertainties of fit reported were calculated by *ATHENA* and *Artemis* as R-Factor = $\Sigma(data – fit)^2 / \Sigma(data^2)$ and chi-squared.

Fourier-transform Infrared Analysis (FTIR)

The FTIR spectra were recorded at the Instituto Andaluz de Ciencias de la Tierra (Granada, Spain) on a Perkin-Elmer Spectrum One FTIR spectrometer (Waltham, Massachusetts, USA) in absorbance mode (4000 to 400 cm^{-1} range) with a resolution of 4 cm^{-1}. Samples were prepared as KBr pressed pellets by diluting 1 mg of sample in 150 mg of dried KBr (Merck, Darmstadt, Germany). The pellets were heated overnight at 120^oC before analysis.

RESULTS

XRD

Each of the seven synthesis experiments produced crystalline phases with 00*l* peaks that are consistent with the presence of serpentine group minerals as the dominant solid phase in the powders (Fig. 1). None of the powders exhibited change in XRD patterns with ethylene glycol solvation. The synthesis involving only Mg and Si as cations (Serp 1) resulted in 00*l* peaks at 7.5 to 7.6 Å (001), 3.65 Å (002), and 1.84 Å (004). The 060 peak occurs at 1.53 Å and the 020 peak is at 4.52–4.54 Å; the 060 indicates a trioctahedral *b*-axis spacing of 9.12 Å whereas the 020 peak indicates a 9.04 to 9.08 Å *b* dimension consistent with trioctahedral but also smaller than typical serpentine group minerals. The strong peak at 2.57 Å is probably the 202 peak and the weaker peak between 1.73 and 1.70 Å is likely to be the 206 peak (Brindley & Brown 1980). The low-angle shoulder on the 001 peak and the non-integer relationship of 001 to higher-order 00*l* peaks (mainly the higher-than-normal 7.5 to 7.6 Å 001 peak) indicated randomly interstratified 2:1 layers (Moore & Reynolds 1997) with structure and composition akin to talc or kerolite. Modeling XRD patterns as an R0 interstratified mineral with 85% serpentine layers and 15% talc layers reproduced the low-angle asymmetry and ~7.5 Å position of the 001 peak and the high-angle asymmetry of the 002 peak (Fig. 1B). One place where the model was not a perfect match was the 0.07 Å difference in position of the 002 peak. The spacing of the broad serpentine 001 peak (~7.5 Å) was between nominal (end-member) 001 spacings of serpentine (7.3 Å) and talc (9.3 Å). The high-angle asymmetry of the 002 peak indicated that it was a composite peak between nominal serpentine 002 (3.65 Å) and talc 003 (3.1 Å) peaks. This type of peak shifting and asymmetry was predicted by the interstratification model developed by Méring (1949) (see also Moore & Reynolds 1997).

Five of the seven powders – Serp 1, Serp 2, Serp 3, Serp 5, and Serp 7 – yielded XRD patterns that were virtually identical to each other, including the pure Mg-Si end-member (i.e. Serp 1). Two of the specimens, however, displayed some notable variations relative to the other five powders – these were Serp 4
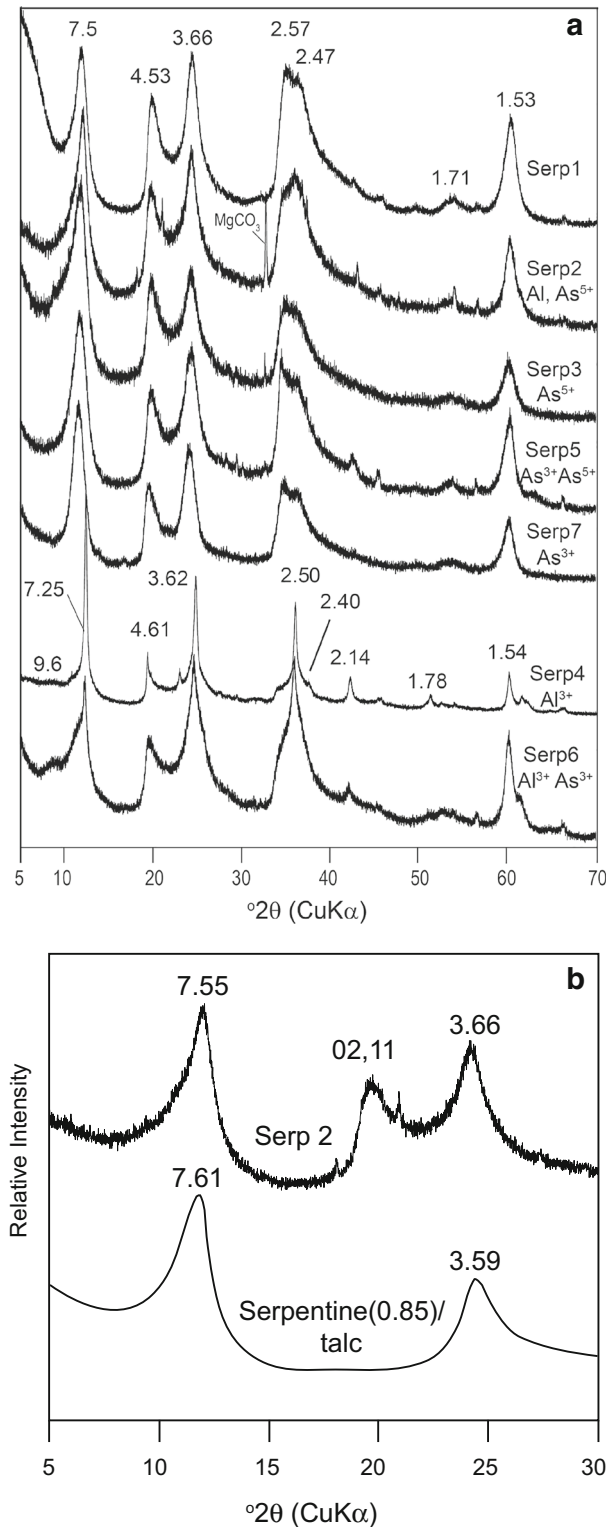
Fig. 1 (**a**) XRD data of random mounts of seven powders produced by synthesis. Data shown are for the air-dried state, digits above peaks indicate spacing in Å, and ions in addition to Mg and Si are listed with sample IDs on the right; (**b**) XRD data from specimen Serp 2 and a model of R0 interstratified serpentine(0.85)/talc. The model does not show a 02,11 peak because *NEWMOD* models 00*l* peaks (*Newmod 2*). The 02,11 in the experimental data is a consequence of the tubular crystal form.

(containing Al in addition to Mg and Si) and Serp 6 (containing both Al^{3+} and As^{3+} in addition to Mg and Si). Serp 4 and Serp 6 were characterized by sharper 00*l* peaks than the others, as well as an 001 peak that occurred at a smaller spacing than the others: 7.25 Å (Serp 4) and 7.22 Å (Serp 6) vs ~7.5 Å for the other 5 powders. Serp 4 had a comparatively sharp 020 peak at 4.61 Å and the 020 peak from Serp 6 occurred at 4.59 Å, peaks consistent with a larger trioctahedral *b*-axis dimension of ~9.2 Å (compared to the other five synthesized powders). The position of the 001 peak was sensitive to Al content (Serna et al. 1979) – in the case of pure Mg-Si (Al-free) serpentines, the 001 occurs at 7.32 Å, but with increasing Al, the 001 spacing decreased, reaching a low of 7.15 Å for serpentines containing 1.0 Al per $O_5(OH)_4$ unit formula. Based on empirical data from Serna et al. (1979), peak positions of 7.25 Å for Serp 4 and 7.22 Å for Serp 6 correspond to ~0.4 to 0.5 Al per $O_5(OH)_4$ unit formula, respectively. The presence of broad and relatively weak peaks at 9.5 Å in addition to serpentine peaks described above indicated the presence of a polyphase mixture dominated by serpentine but also containing discrete packets of talc- or kerolite-like 2:1 layers, likely as zones within serpentine crystals, or as discrete talc-like crystals.

TEM

Morphologically, the majority of crystals produced by the synthesis reactions were tubular (Serp 1, 2, 3, 5, and 7); tube length was ~2000 Å (0.2 µm), and tube diameter was ~200 Å (Fig. 2), with one exception, Serp 3, where tube length was <500 Å and crystals were difficult to image due to instability under the electron beam. The two specimens that were distinct in XRD analysis, Serp 4 (containing Al^{3+}) and Serp 6 (containing Al^{3+} and As^{3+}), were also distinct in the TEM, consisting of platy crystals 1000–2000 Å in diameter and 100 to 200 Å thick, often hexagonal with either rounded or sharp edges.

Analysis by EDX of dozens of crystals indicated that some were stoichiometrically serpentine-group minerals, yet others contained excess Si which suggested the presence of 2:1 layers interstratified with 1:1 serpentine layers (Table 2). Measurements of crystal chemistry (single crystals) were summarized individually from Serp 1 through Serp 7, and mineral formulas are presented on the basis of $O_5(OH)_4$ units; so for an ideal 1:1 clay, the sum of charges of cations is +14. Anything <14 implies vacancies or interstratified 2:1 layers. In terms of speciation, Al is commonly partitioned preferentially into the octahedral sheet, a decision based on analyses of natural serpentines which has shown that octahedral Al is often greater than tetrahedral Al (e.g. Fuchs et al. 1998; Deer et al. 2009). Partitioning Al into the octahedral sheet also produces compositions that are most consistent with the large ratio of serpentine to talc layers observed in all of the analytical methods. Partitioning Al into the tetrahedral sheet would elevate the number of tetrahedral sites, resulting in a greater abundance of 2:1 layers than was indicated by XRD and HRTEM results in the present study. This dominantly octahedral apportionment of Al resulted in the unit-cell compositions shown, but it did not rule out the potential for tetrahedral Al in cases where it

was not shown. All arsenic, whether As^{5+} or As^{3+}, was partitioned into the tetrahedral sheet (Hattori et al. 2005).

- Serp 1, synthesized with only Mg and Si as cations (no Al or As), had molar Mg:Si ratios ranging from 1.1 to 1.4, where 1.5 is ideal for a serpentine with $Mg_3Si_2O_5(OH)_4$ stoichiometry, and 0.75 is ideal for a talc 2:1 layer. The average Serp 1 was a Mg-deficient tubular crystal with mean composition $Mg_{2.6} Si_{2.0} O_5(OH)_4$. The lack of Mg relative to Si led to a total cation charge of +13.2, consistent with ~15% interstratified 2:1 layers, as indicated by XRD data and HRTEM (below). Using terminology for interstratified clay minerals (Moore & Reynolds 1997), these could be described as "serpentine(0.85)/talc."

- Serp 2 contained Mg-deficient tubular crystals with mean composition ~$Mg_{2.3}Al_{0.16}(Si_{1.9}Al_{0.08} As^{5+}_{0.04})O_5(OH)_4$. The sum of octahedral and tetrahedral charge was ~ +13.2 (where +14 is ideal serpentine), and the deficiency appeared to be in the octahedral sheet, where the sum of charges was +5.14 (+6.0 is the ideal Mg_3 end-member). In Serp 2, the mean tetrahedral charge was +8.04. The small octahedral charge implied the presence of interstratified talc-like layers (~15%), much like Serp 1. This is the only Al-bearing specimen occurring as chrysotile-like tubes rather than platy crystals.

- Serp 3 contained tubular crystals with a mean composition of $Mg_{2.6} (Si_{1.98} As^{5+}_{0.02})O_5(OH)_4$, very similar to Serp 1, with a deficiency of Mg consistent with some interstratified talc-like layers. Similar to Serp 1 and Serp 2, the Mg:Si ratio of 1.3 was consistent with ~15% 2:1 talc-like layers in interstratified serpentine/talc. The tubular crystals in this specimen were much finer grained than in the other six; the majority had tube lengths <500 Å, making it difficult to obtain images or compositional analyses due to instability. As was detected in only two crystals (of 11).

- Serp 4 consisted of Al-bearing platy crystals the mean formula of which, if all Al was partitioned into octahedral sites, was $(Mg_{1.76}Al_{0.72})(Si_{2.0})O_5(OH)_4$ and the cation charge was +13.7 (and if some Al were partitioned into tetrahedral sites, cation charge would drop further below the ideal value of +14.0). This charge deficiency (i.e. < +14.0) is consistent with a deficiency of octahedral sheets relative to tetrahedral sheets, implying the presence of talc-like 2:1 layers. Some single crystals produced compositions such as $(Mg_{2.40}Al_{0.43})(Si_{1.91}Al_{0.09})O_5(OH)_4$ where the ideal total charge is +14.0 for a serpentine-group mineral. In other crystals, compositions did not cast well as serpentines, e.g. $(Mg_{1.87}Al_{0.38})(Si_{2.36})O_5(OH)_4$, stoichiometry which for this individual crystal indicated the occurrence of talc-like layers in a ~60% serpentine:40% talc proportion. Overall, Serp 4 contained ~10% talc layers.

- Serp 5 contained tubular crystals for which the mean composition was $Mg_{2.79} (Si_{1.81} As_{0.20}) O_5(OH)_4$. Assuming equal amounts of As^{3+} and As^{5+} in tetrahedral sites, cation charges summed to +13.6, a low value compared to the ideal +14.0 for a 1:1 clay. If all As were As^{5+}, the cation charge sum would be +13.8. Values <14 indicate a 1:1 to 2:1 layer ratio that is smaller than that of an ideal serpentine, consistent with ~10% interstratified talc-like layers. Compositions of selected single crystals ranged from electrically neutral serpentine group stoichiometry, e.g. $Mg_{2.9} (Si_{1.64} As_{0.36}) O_5(OH)_4$, to crystals that appeared to be deficient in

TUBULAR SERPENTINES
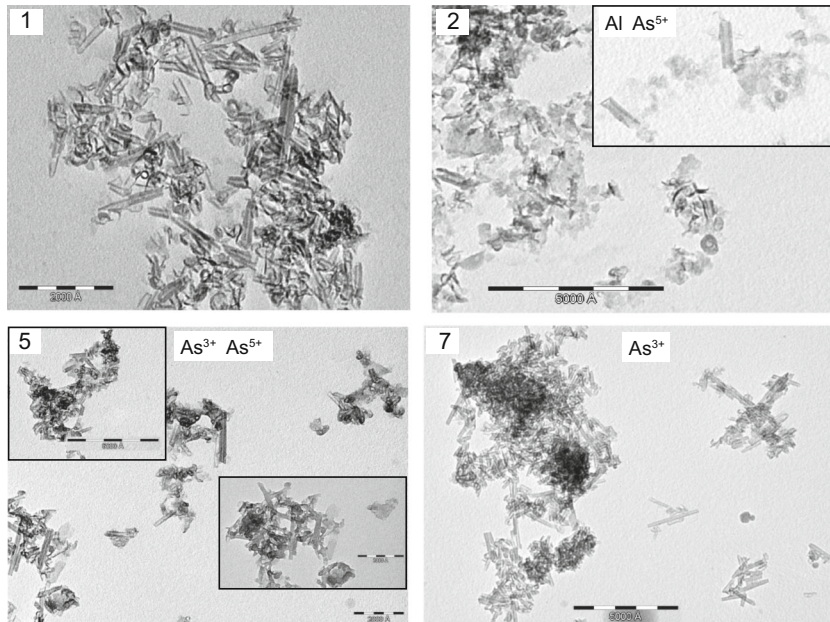
PLATY SERPENTINES
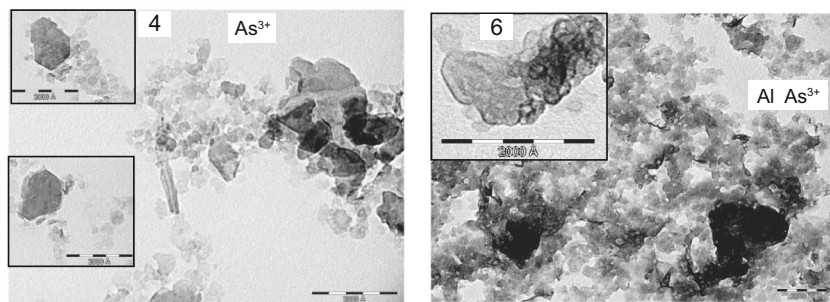
Fig. 2 TEM images of tubular serpentines (Serp 1, Serp 2, Serp 5, Serp 7, top four images) and platy serpentines with hexagonal morphology (Serp 4, Serp 6). Serp 3 (not shown) is also tubular, but is distinct in its very fine size, making it difficult to image crystals compared to the six specimens shown here.

octahedral sheets for a serpentine group mineral, e.g. $(Mg_{2.44})(Si_{2.28}As_{0.11})O_5(OH)_4$. This was clearly not a stoichiometrically correct serpentine, and a reasonable explanation is the presence of interstratified talc-like layers in the dominantly serpentine mineral, consistent with XRD data. The most As-rich crystal analyzed by TEM-AEM had a composition of $(Mg_{2.38})(Si_{1.37}As^{5+}_{0.51} As^{3+}_{0.12})O_5(OH)_4$, where As oxidation states were apportioned based on XANES data.

- Serp 6 contained sub-hexagonal platy crystals with mean composition $(Mg_{2.07}Al_{0.52}) (Si_{1.97}As^{3+}_{0.03}) O_5(OH)_4$. The sum of cationic charges was +13.7, consistent with ~10% talc-like 2:1 layers. The crystal with the largest As concentration had a formula of $(Mg_{2.22}Al_{0.56}) (Si_{1.89}As^{3+}_{0.11}) O_5(OH)_4$ and the sum of cation charges was +14.0.
- Serp 7 contained tubular crystals with an average formula $(Mg_{2.66}) (Si_{1.97}As^{3+}_{0.03}) O_5(OH)_4$, yielding a cation charge sum of +13.3 that implied ~15% talc-like layers in single crystals. Interestingly, the two crystals with the

largest As contents produced stoichiometries closest to 1:1 trioctahedral serpentine stoichiometry: $(Mg_{2.98}) (Si_{1.93}As^{3+}_{0.07}) O_5(OH)_4$ and $(Mg_{2.96}) (Si_{1.86}As^{3+}_{0.14}) O_5(OH)_4$. Cation charge sums for these two were +13.9 and +13.8, respectively.

The HRTEM images of vertically oriented tubular crystals revealed diameters (perpendicular to the vertical *b* axis) of 150 to 200 Å with central holes of ~120 to 160 Å diameter. The rolled layers had thicknesses of 36 to 45 Å (Fig. 3a), but instability of the crystals in the presence of the electron beam prevented precise analysis of the layer structure. Crystals where the rolled layers were a total of 36 Å thick likely consisted of five stacked 1:1 7.2 Å layers; in other cases (e.g. thickness of 45 Å), these zones possibly contained five 1:1 serpentine layers and one 2:1 talc layer. While determining precisely the presence of interstratified 2:1 layers was not possible with HRTEM, this suggestion is consistent with

Table 2 Concentrations of the cations used in synthesis, presented in g kg^{-1} for idealized synthesis stoichiometry ("Stoich"), as well as results of chemical analysis by TEM-EDS and ICPMS. These values are for hydrous serpentine where the $O_5(OH)_4$ component accounts for 520 ± 10 g/kg (variability depends on mass of cations). Si could not be analyzed by ICPMS. Sample IDs with "TU" indicate tubular crystals and "PL" indicates platy crystals

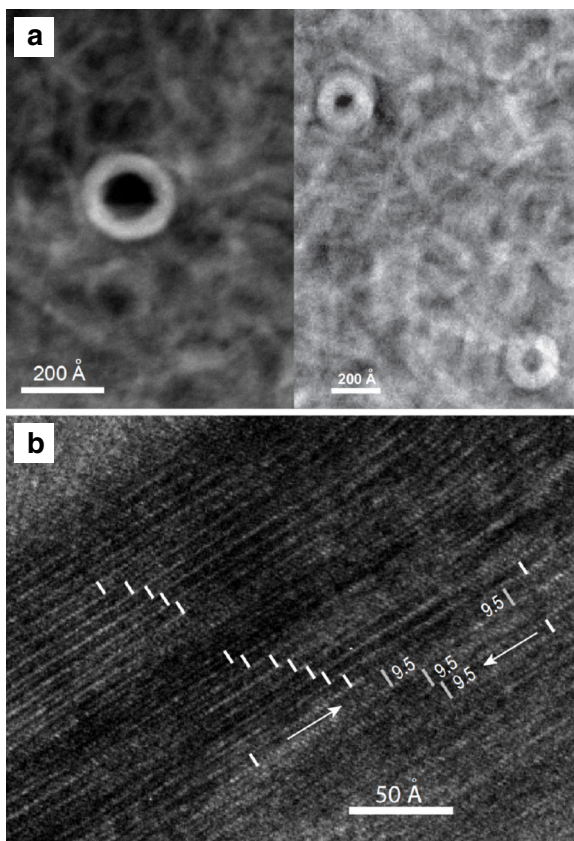| ID	Molar Mass (g/mol)	Mg (g/kg)			Al (g/kg)			Si (g/kg)			As (g/kg)		
		Stoich	TEM-EDS	ICPMS	Stoich	TEM-EDS	ICPMS	Stoich	TEM-EDS	ICPMS	Stoich	TEM-EDS	ICPMS
Serp1 TU	277.1	263	246	252	0.0	< 1	< 1	203	219	--	0.0	< 1	< 1
Serp2 TU	279.9	261	238	260	5.8	23.1	5.1	189	227	--	16.1	12.7	6.2
Serp3 TU	283.0	247	246	222	0.0	< 1	< 1	187	218	--	31.8	1.2	14.1
Serp4 PL	273.2	262	171	134	11.9	77.5	9.1	199	224	--	0.0	< 1	< 1
Serp5 TU	282.7	263	246	205	0.0	< 1	< 1	191	182	--	31.8	21.1	11.3
Serp6 PL	280.1	259	196	237	5.8	54.6	4.5	197	215	--	16.0	8.7	8.5
Serp7 TU	282.7	256	251	219	0.0	< 1	< 1	189	214	--	32.3	8.6	14.7

XRD and TEM-AEM compositional measurements. In the case of platy hexagonal crystals, the majority of *c*-axis spacings were 7 Å but clear examples of clusters of interstratified ~ 9.5 Å layers were also visible (Fig. 3b), including lateral

Fig. 3 HRTEM images showing (**a**) cross-sections of vertical tubular crystals in Serp 5 showing the thickness of rolled layers as well as the diameter of the central hole; and (**b**) interstratification of 7 Å and 9.5 Å layers in a platy crystal from Serp 4 that was oriented vertically to emphasize *c*-axis spacings.

transitions between 1:1 (7 Å) layers and 2:1 (9.5 Å) layers. This evidence for serpentine with packets of interstratified talc is consistent with XRD and TEM-AEM data.

ICPMS of Dissolved Serpentine Powders

Data from ICPMS (Table 3) provided information on Al, As, and Mg content of dissolved serpentines. Like TEM-AEM, analysis by ICPMS revealed the presence of Al and As at measureable levels in tubular and platy serpentines; unlike TEM, ICPMS analysis did not return reproducible results for Si, a problem attributed to low solubility of Si. Comparison of Al measured by TEM-EDS and ICPMS showed that TEM Al measurements were larger than those reported by ICPMS by up to an order of magnitude. Buffering of aqua regia solutions during dissolution of serpentine crystals could lead to formation of nano-scale Al hydroxides that were filtered prior to ICPMS analysis, thus producing an anomalously low bias to ICPMS Al data. Considering elemental As concentration in the synthesized crystals, TEM average values were sometimes larger than ICPMS (e.g. Serp 2 and 5), they were equal in one case (Serp 6), and lower in two specimens (Serp 3 and 7). In Serp 3, ICPMS detected As at 14.1 g/kg while TEM returned an average ($N = 11$) of only 1.2 g/kg, resulting from As detected in only two Serp 3 crystals in TEM. These differences were, at least in part, due to the small sample size of TEM analyses of single crystals ($N = 7$ to 12 per specimen) compared to analysis of a dissolved mineral powder in the case of ICPMS. Serp 3 consisted of many tubular nanoparticle serpentines (<20 nm) that were difficult to image and were unstable under the electron beam. Low Mg in Serp 4 measured by ICPMS may indicate incomplete dissolution of this particular powder when preparing the solution for analysis, which would also contribute to low Al measurement by ICPMS.

If ICPMS results reflect the mean composition of dissolved serpentine, then they present a more representative analysis of average mineral composition. The problem is that pre-ICPMS dissolution may incorporate phases other than serpentine, or be affected by incomplete dissolution. The advantage of TEM-AEM is the capacity to determine the composition of individual crystals, but there is no guarantee that they encompass the full

Table 3 Comparison of TEM-AEM to ICPMS analysis of mineral composition. In all cases, formulae are presented relative to an idealized $O_5(OH)_4$ unit cell, and in many cases, the sum of cationic charges is <14, a consequence of interstratified talc layers

	TEM-AEM	ICPMS
Serp 1	$Mg_{2.6}Si_{2.0}O_5(OH)_4$	$Mg_{2.6}Si_2O_5(OH)_4$
Serp 2	$Mg_{2.3}Al_{0.16}(Si_{1.88}Al_{0.08}As^{5+}{}_{0.04})O_5(OH)_4$	$Mg_{2.6}Al_{0.05}(Si_{1.98}As^{5+}{}_{0.02})O_5(OH)_4$
Serp 3	$Mg_{2.6}(Si_{1.98}As^{5+}{}_{0.02})O_5(OH)_4$	$Mg_{2.2}(Si_{1.96}As^{5+}{}_{0.04})O_5(OH)_4$
Serp 4	$(Mg_{1.76}Al_{0.72})Si_{2.0}O_5(OH)_4$	*$(Mg_{1.3}Al_{0.4})Si_2O_5(OH)_4$*
Serp 5	$Mg_{2.8}(Si_{1.8}As^{5+}{}_{0.16}As^{3+}{}_{0.04})O_5(OH)_4$	$Mg_{2.2}(Si_{1.94}As^{5+}{}_{0.05}As^{3+}{}_{0.01})O_5(OH)_4$
Serp 6	$(Mg_{2.07}Al_{0.52})(Si_{1.97}As^{3+}{}_{0.03})O_5(OH)_4$	$(Mg_{2.5}Al_{0.14})(Si_{1.97}As^{3+}{}_{0.03})O_5(OH)_4$
Serp 7	$(Mg_{2.66})(Si_{1.97}As^{3+}{}_{0.03})O_5(OH)_4$	$Mg_{2.2}(Si_{1.94}As^{3+}{}_{0.06})O_5(OH)_4$

range of compositions for a powder sample, nor necessarily a representative average. What is clear in this study is that repeatable TEM-AEM measurements of single crystals provide reliable evidence of Al and As in tubular and platy serpentines, and the occurrence and magnitude of Al and As in these samples is supported by ICPMS analysis of dissolved powders.

XANES/XAFS

The normalized As K-edge XANES spectra obtained from Serp 5 and the liquid standards of As^{5+} and As^{3+} (Fig. 4a) indicated the predominance of As^{5+} (over As^{3+}) (Table 4) in a synthesis experiment that contained equal amounts of those two species in the original synthesis solution. E_0, measured as the white line, was found to be 11875.1 eV (As^{5+}), 11871.7 eV (As^{3+}), and 11874.8 eV (Serp 5). By fitting Serp 5 to the liquid standards using linear combination fitting in *ATHENA* (Table 4), the sample was 78% As^{5+} and 22% As^{3+} (Arai et al. 2001; Takahashi et al. 2003; Ravel & Newville 2005; Müller et al. 2010). The small R-Factor of 0.016 indicates the goodness of fit (Ravel & Newville 2005; Liu et al. 2008). Considering XANES data, the mean molar formula unit of Serp 5 was $Mg_{2.8}(Si_{1.8}As^{5+}{}_{0.16}As^{3+}{}_{0.04})O_5(OH)_4$.

Arsenic K-edge XAFS analysis was utilized to investigate the position of As within the clay structure. The XAFS spectra in *R* space for Serp 5 (solid line) and fitted to theoretical standards (dashed line) are shown in Fig. 4b. Background removal, normalization, and Fourier transform were performed using the *ATHENA* program (Newville 2001). For the Fourier transform, a Hanning window was used with a *k* range of 2.7 to 12.2 $Å^{-1}$ and a k^3 weighting. The XAFS fitting was done using the *Artemis* program (Ravel & Newville 2005) from an *R* range of 1 to 3.5 Å. The theoretical scattering paths used in the fitting were generated using the *FEFF 9.0* calculation code (Rehr et al. 2010) based on an antigorite structure with As substituted for a Si atom within the tetrahedral sheet (Dódony et al. 2002). During the fitting, only single scattering paths were considered. The amplitude reduction factor, $S_0{}^2$, was fixed at 0.96, the value obtained from fitting the XAFS spectrum for $Na_2HAsO_4·7H_2O$.

The first shell was fitted successfully as As-O with a coordination number of 3.3 and an interatomic distance of 1.71 Å (Fig. 4b, Table 5). The second shell was fitted

successfully as As-Si with a coordination number of 3 and an interatomic distance of 3.20 Å and As-Mg with a coordination number of 3 and an interatomic distance of 3.45 Å. These fits agreed with XANES results indicating that both As^{5+} and As^{3+} were present in the tetrahedral sheet of Serp 5, As^{5+} with a tetrahedral coordination to four O atoms, and As^{3+} with a trigonal pyramid coordination to three O atoms, both with coordination to three Si within the tetrahedral sheet and three Mg within the octahedral sheet. Further analysis via Si K-edge XAFS would help to further probe the presence of tetrahedral
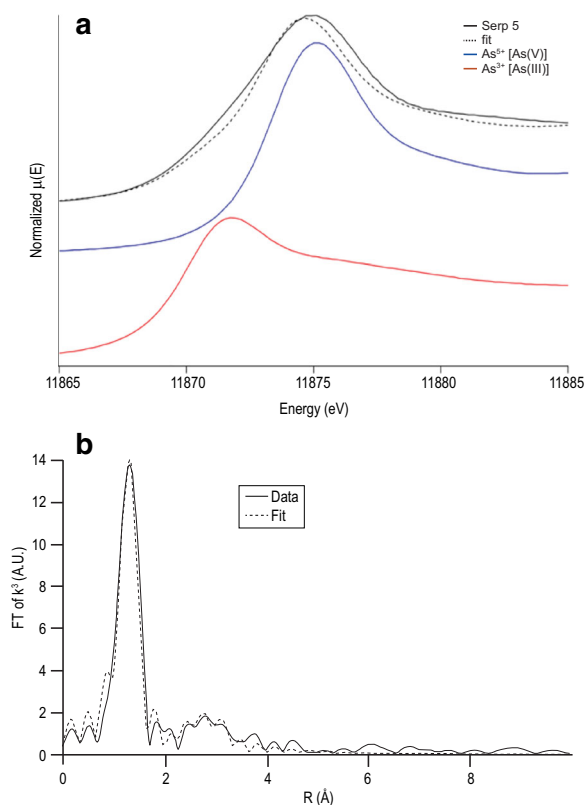
Fig. 4 XAS data: (**a**) Stacked, normalized, flattened As K-edge XANES spectra for Serp 5 and liquid standards of As^{5+} and As^{3+}. The dashed line indicates a fit determined via LCF; (**b**) As K-edge XAFS spectra of Serp 5 as the Fourier transform of the $k^3 * \chi(k)$. Solid lines indicate raw data and dashed lines the fit to theoretical standards.

Table 4 Results of linear combination fitting showing combinations of standards yielding the best fits to arsenic K-edge XANES

Sample name	XANES individual components		
	As^{5+} [a]	As^{3+} [a]	R-Factor[b]
Serp 5	78 ± 1.5	22.0 ± 1.5	0.016

Note: [a] Uncertainties of fit reported were calculated by *Athena*.

[b] R-Factor = $\Sigma(data - fit)^2 / \Sigma(data^2)$. R-factor is given as the error measure, but expressed as chi-squared, in this case, 1.666. Liquid standards of As^{5+} and As^{3+} were used as the standards for As (III) and As (V) components, respectively.

Al and its relationship to As in the tetrahedral sheet. The calculated R-factor of 0.016 showed the relative goodness of fit, with good fits defined as R <0.05 (Liu et al. 2008). Online Resource 1 presents a K-edge EXAFS k3 * χ(k) spectrum of Serp 5.

FTIR

Tubular serpentines The infrared spectra of the synthesized tubular serpentines contained a strong 980 cm^{-1} peak that corresponds to Si–O stretching (Si and basal oxygen of the tetrahedral sheet, approximately parallel to the *a-b* plane) and a 1087 cm^{-1} peak caused by Si–O stretching (Si and apical oxygen, perpendicular to *a-b* plane) (Fig. 5). Serp 2 differed slightly from the other tubular synthesized powders in that the basal Si-O stretching peak occurred at 1003 cm^{-1} (rather than 980 cm^{-1}). The 3697 cm^{-1} peak in the tubular serpentine spectra was produced by stretching of the OH bond in the presence of 3 Mg per hexagonal ring in the octahedral sheet (Mg$_3$O-H), and the weak shoulder at 3640–3648 may be related to octahedral vacancies.

The infrared spectra of the synthesized tubular serpentines were similar to those of natural chrysotiles (Farmer 1974; Craw et al. 1987; Suquet 1987; Rozalén et al. 2014), especially in terms of the strong 980 cm^{-1} basal Si-O stretching vibration and the Mg$_3$O-H vibration at 3697 cm^{-1} (Table 6). Natural chrysotiles produce a basal Si–O peak that ranges from 980 cm^{-1} (Farmer 1974; Craw et al. 1987) to 960 cm^{-1} (Yariv & Heller-Kallai 1975; Suquet 1987; Rozalén et al. 2014). Natural chrysotiles produce a Mg$_3$O-H vibration at 3695 ± 5 cm^{-1}. The ~1020 cm^{-1} shoulder on the 960–980 cm^{-1} peak is probably related to Si–O stretching in tetrahedral sheets of small amounts of talc-like or kerolite-like 2:1 layers (e.g. Farmer 1974; Čavajda et al. 2015). Spectra of tubular crystals with the greatest amount of As (Serp 5, Serp 7) contained a small peak at 880 cm. Peaks that occur in the ~590–640 cm^{-1} range in synthesized samples in the present study and in natural chrysotiles are probably related to vibrations of the Mg–OH bond in the octahedral sheet (Suquet 1987).

Platy serpentines The platy specimens (Serp 4 and Serp 6) produced spectra that were distinct from the tubular forms and similar to synthesized Al-bearing Mg-serpentines that contain 0.2 to 1.0 Al per O$_5$(OH)$_4$ (Serna et al. 1979), and natural antigorite with ~0.2 Al per per O$_5$(OH)$_4$ (Mellini et al. 2002). Those synthesized in the current study produced a strong basal plane Si–O stretching peak at 1007 cm^{-1} (Serp 4) or 1003 cm^{-1} (Serp 6), similar to the 995 cm^{-1} peak of synthesized Mg-serpentines of Serna et al. (1979), or the 987 cm^{-1} Si–O basal vibration from natural antigorite (Mellini et al. 2002). The shift in this peak towards higher wavenumbers in the synthesized serpentines was likely caused by interstratified talc layers that pull the Si-O stretching peak towards 1020 cm^{-1} (Farmer & Russell 1967).

The 3662 and 3660 cm^{-1} Mg–OH hydroxyl stretching peak for Serp 4 and Serp 6 corresponds to the 3660 cm^{-1} peak for serpentine with 0.4 Al per O$_5$(OH)$_4$ unit formula (Serna et al. 1979), and the position of this peak is sensitive

Table 5 EXAFS fit parameters for Serp 5 and As^{5+} and As^{3+} liquid standards

Sample	R factor [a]	S$_0^2$ [b]	E$_0$ [c]	EXAFS fit parameters								
				First shell, As-O			Second shell, As-Si			Second shell, As-Mg		
				R (Å) [d]	N [e]	σ^2(Å)^2 [f]	R (Å) [d]	N [e]	σ^2(Å)^2 [f]	R (Å) [d]	N [e]	σ^2(Å)^2 [f]
Serp 5	0.016	0.96*	10.3	1.71	3.30*	0.002	3.2	3.00*	0.011	3.45	3.00*	0.007

Note: [a] R-Factor = $\Sigma(data - fit)^2 / \Sigma(data^2)$
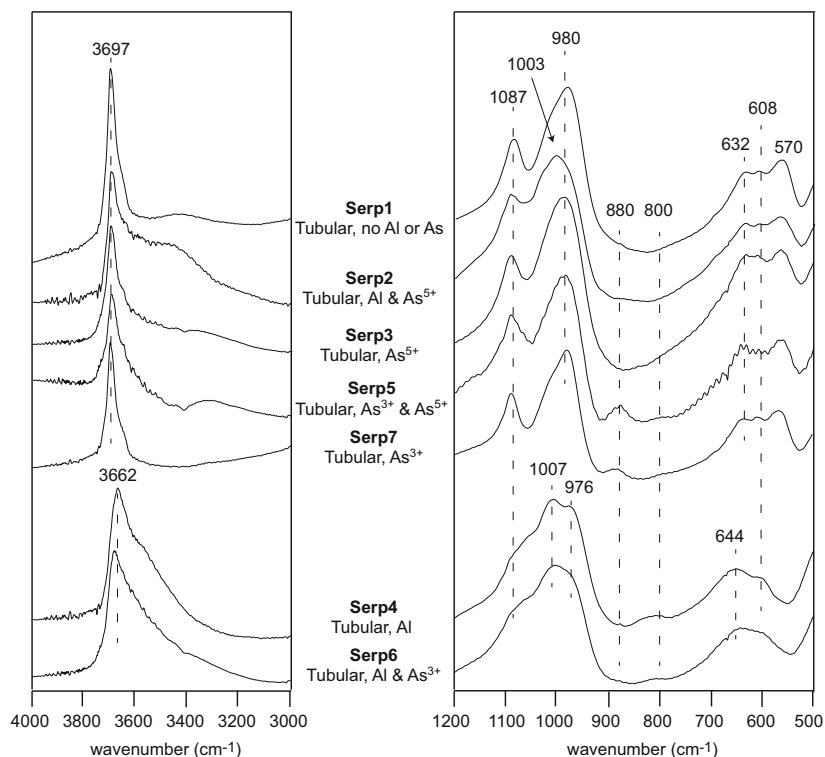
[b] amplitude reduction factor

[c] energy shift

[d] interatomic distance

[e] coordination number

[f] Debye-Waller factor

*fixed parameter.

Fig. 5 FTIR spectra of the synthesized serpentine group minerals. Peak positions are indicated in units of cm^{-1}.

to Al, migrating to lower wavenumbers with increasing Al. The peak position for serpentines with no Al is 3685 cm^{-1}, whereas the peak for serpentines with 1.0 Al per $O_5(OH)_4$ unit formula is at 3650 cm^{-1}. This peak occurs at 3678 in natural antigorite with 0.16 Al (Mellini et al. 2002), also consistent with this effect. Thus, the 3660 position is consistent with 0.4 to 0.5 Al per $O_5(OH)_4$ unit formula in the octahedral sheet (TEM-AEM, for reference, indicates 0.5 to 0.7 Al per $O_5(OH)_4$). The 608 and 644 cm^{-1} peaks were probably caused by Mg-OH vibrations in the chrysotile octahedral sheet (Farmer 1974). The weak 800–810 cm^{-1} peak may have been produced by tetrahedral Al given that it occurs in synthesized Al-bearing serpentines from the current study as well as those of Serna et al. (1979), and in Al-bearing lizardite (Viti & Mellini 1997). If the peaks between 800 and 900 cm^{-1} were to represent vibrations in the tetrahedral sheet corresponding to greater bond length or instability compared to Si–O bonds, they may be a signal of Al or As. Theoretically, peaks corresponding to As^{5+} in the tetrahedral sheet would fall between Si–O (~1000 cm^{-1}) and Al–O (~800 cm^{-1}; Serna et al. 1979). The FTIR peak at 880 cm^{-1} (Fig. 5) appeared most prominently in the two synthesized tubular serpentines with the greatest As content, Serp 5 and Serp 7. In serpentines with smaller amounts of As, this peak was barely detectable. Four compounds with tetrahedral coordination of As^{5+} that contain peaks in this range are: AsO_4^{3-}, with v1 symmetric stretching at 810–837 cm^{-1} and v2 anti-symmetrical stretching at 810–878 cm^{-1}; Ca_3AsO_4, with v1 symmetric stretching at 840 cm^{-1} and v2

anti-symmetrical stretching at 880 cm^{-1} (Farmer 1974); $FeAsO_4$, with a v1 symmetric stretching at 823 cm^{-1} (Chukanov 2014); and $PbAl_3(AsO_4)_2(OH)_5 \cdot H_2O$, with a composite v1 symmetric stretching/v2 anti-symmetrical stretching at 830–840 cm^{-1} (Frost et al. 2013). Modeling indicates that the As-O stretching vibration caused by tetrahedral AsO_4^{3-} in crystalline solids should occur in the range 820–960 cm^{-1} (Myneni et al. 1998), where the variability depends on coordination to other species in the mineral structure.

DISCUSSION

Crystallochemical Characterization of the Synthesized Serpentines

The main mineral structure formed by the synthesis experiments was trioctahedral Mg phyllosilicate dominated by 1:1 layers with the capacity to incorporate arsenic into tetrahedral sites. Data from XRD, TEM, and FTIR indicated that the synthesized powders – whether tubular or platy – consisted mainly of 1:1 layers (serpentine) with 10–15% talc-like 2:1 layers, which in tubular crystals was randomly interstratified and in platy crystals occurred as discrete packets. Evidence for the occurrence of 2:1 layers included TEM images and compositions, lattice spacings of ~9.5 Å in electron diffraction, XRD data of tubular crystals indicating 15% randomly interstratified talc-like 2:1 layers in a dominantly 1:1 mineral, XRD data of platy crystals showing a broad ~9.5 Å peak caused by discrete packets of talc-like layers, and XRF data that showed

Table 6 FTIR peaks (cm^{-1}) for tubular and platy serpentines synthesized for this study compared to data from natural chrysotile (Craw et al. 1987; Farmer, 1974; Rozalén et al. 2014, Suquet, 1987), antigorite (Mellini et al. 2002), and lizardite (Viti & Mellini, 1997), as well as serpentine synthesized by Serna et al. (1979)

	Tubular serpentines (this study)					Natural chrysotiles				Platy Serp (this study)		Synth Serp	Antigorite	Lizardite
	Serp 1	Serp 2c	Serp 3c	Serp 5c	Serp 7C	Craw	Farmer	Rozalen	Suquet	Serp 4c	Serp 6c	Serna79	Mellini02	V+M 97
Mg$_3$O-H	**3697**	**3697**	**3696**	**3696**	**3698**	**3697**	**3697**	**3690**	**3700**	**3662**	**3660**	**3660**	**3678**	**3685**
O-H - vac / Al	3649 wk sh	3640 wk sh	3644 wk sh	3646 wk sh	3648 wk sh	3650	3651	3645 sh	3651	--	--	--	--	3586
H$_2$O ads	3459 br	--	3465	3465	3466	3500	--	--	--	3501	3467	3460	--	3440
Si-apical	1087	1091	1089	1089	1089	--	1080	1086	1082	1080 sh	1080 sh	1050	1083	1088
Si-basal	--	--	--	--	--	--	1020	--	1025 sh	**1007**	**1003**	**995**	**987**	985 sh
Si-basal	**980**	**1003**	**984**	**983**	**979**	**980**	**980**	**962**	**960**	976 sh	976 sh	**970**	970 sh	**952**
See text	--	--	--	876	880	--	--	--	--	880 wk	--	--	--	--
See text	--	--	800 wk	--	800 wk	--	--	--	--	800 wk br	800 wk br	810 wk	--	805 wk
Mg$_3$-OH	631	632	632	632	632	--	634 sh	--	--	644	644	**645**	638 sh	--
Mg$_3$-OH	608	608	608	608	608	**590**	**604**	**604**	**605**	608	608	610 sh	**619**	**617**
Si-O bending	570	570	570	570	570	--	588	558 sh	552 wk	--	--	525 wk	568	--
XRD 001	7.5 Å br	7.5 Å br	7.5 Å br	7.5 Å br	7.5 Å br	7.35 Å	NA	7.3 Å	NA	7.22 Å	7.25 Å	--	7.26	7.23 Å
Al or As	No Al or As	Al > As^{5+}	tr As^{5+}	As^{5+} > As^{3+}	As^{3+}	0.09 Al	NA	0.06 Al	0.01 Al	Al	Al > As^{3+}	0.4 Al	0.16 Al	0.16 Al

sh = shoulder; wk = weak; br = broad; tr = "trace" i.e. < 0.03 p. f. u. (O$_5$(OH)$_4$), and Al values in the bottom row are p. f. u. O$_5$(OH)$_4$.

Bold indicates strong stand-alone peak, rather than shoulder, composite peak or weak peak.

evidence of talc layers in spectra otherwise dominated by serpentine.

Morphology, composition and terminology   The tubular morphology and evidence for interstratified talc layers in five of the seven specimens indicated the presence of what could be termed R0 chrysotile(0.85)/talc. The platy crystals in Serp 4 and Serp 6 possessed morphologies, compositions, and mineral structures that contain attributes of antigorite and lizardite. XRD patterns of the platy serpentines indicated that talc-like layers were physically intermixed with serpentine layers, and HRTEM images showed the talc-like layers as clusters within serpentine crystals. With insufficient precision to distinguish antigorite from lizardite layer type, the platy varieties could be termed platy serpentine with talc layers occurring in packets and comprising 10–15% of the crystal. These synthesized crystals are the first known occurrence of interstratified serpentine/talc. For the purpose of brevity, consistency, and context, from this point onward, the terms tubular serpentine and platy serpentine will be used.

The two crystal forms produced in these experiments were the result of variations in crystal radii of the cations in tetrahedral and octahedral sites. The tubular serpentines ranged compositionally from Mg-Si end-member (Serp 1) to crystals containing As (Serp 3, 5, and 7) or a mix of Al and As (Serp 2); the FTIR spectra for these were similar to that of chrysotile. The two specimens with platy crystals contained either Al (Serp 4) or Al and As^{3+} (Serp 6). The FTIR spectra for the platy crystals were more similar to naturally occurring antigorite than lizardite, but the data do not fit either perfectly, suggesting that the platy serpentines may possess elements of both antigorite-like and lizardite-like zones (Table 6).

In end-member Mg-Si serpentine, where the tetrahedral sheet *b*-axis dimension is less than the octahedral *b*-axis dimension, tetrahedral sheets must flex outward to increase distance between apical oxygen atoms and enable them to bond with the octahedral sheet (Deer et al. 2009). Chrysotile contains carpet-like rolls of 1:1 layers, where the octahedral sheets are on the outside of the roll for a given 1:1 layer. Substitution of As^{5+} (0.48 Å) or As^{3+} (0.54 Å) for Si (0.40 Å) at the levels achieved in the current experiments was not sufficient to overcome the tetrahedral-octahedral mismatch, and tubular crystals formed. In the platy serpentines (Serp 4 and 6), Al substitution (perhaps with some inversions) occurred at levels sufficient to overcome the mismatch (Fig. 6).
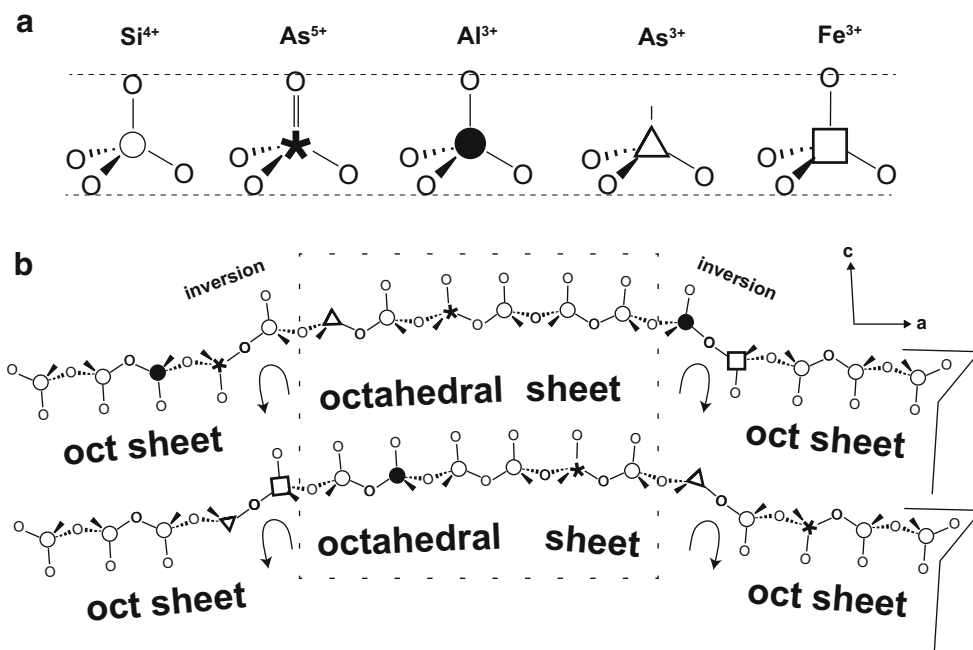
By comparing the concentration of an element in serpentine relative to its concentration in the initial solution (Table 2), the serpentines appeared to strongly partition Al from solution. Similar to the synthesized Al-lizardites of Bentabol et al. (2010), and based on indirect evidence from TEM and FTIR, Al appeared to be partitioned into the octahedral sheet preferentially over the tetrahedral sheet. Si was slightly more concentrated in serpentine relative to the original solution, and Mg was stoichiometrically slightly lower than was targeted in the initial solution (i.e. 3 Mg:2 Si), with the greatest difference noted in the Al-rich Serp 4. Arsenic was also stoichiometrically lower in serpentine than in the initial solution with one exception, the slight partitioning of As^{5+} into Serp 5.

Earlier research has documented compositional overlap among the three main naturally occurring serpentine-group minerals; in general, lizardite and antigorite (i.e. platy forms) have greater Al contents than chrysotile (Deer et al. 2009). This is consistent with the crystals synthesized in this study, where the two platy serpentines contained greater amounts of Al than the tubular serpentines (Fig. 6), and Al in the synthesized platy serpentines occurred at levels comparable to natural Al-rich lizardites and Al-rich antigorites (up to 0.4 Al per $O_5(OH)_4$). In the case of lizardite, Al substitution enables the mineral to satisfy the mismatch, because when substituted for octahedral Mg (0.86 Å), the relatively small Al (0.72 Å) would shrink the octahedral sheet; when substituted for tetrahedral Si (0.40 Å), the relatively large Al (0.53 Å) could expand the tetrahedral sheet. Also, incorporation of Al into the octahedral sheet may lead to vacancies that also would shrink the octahedral sheet. Thus, by means of octahedral and/or tetrahedral substitution, Al can minimize the tetrahedral-octahedral mismatch. Some platy Al-rich serpentines do not solve the mismatch merely by Al substitution, but rather contain a modulating layer structure characteristic of antigorite (Fig. 7).

Insights into arsenic speciation in serpentine   The tubular serpentines are associated with larger As content than the platy serpentines, especially tubular Serp 5 with 2 wt.% As or 20 g kg^{-1} (21 g kg^{-1} by TEM-AEM and 11 g kg^{-1} by ICPMS) in the mineral structure (based on a hydrous $O_5(OH)_4$ composition). This amount is equivalent to 10% of tetrahedral sites occupied by As (up to 0.2 p.f.u. As^{5+}). Serp 3 – with only As^{5+} in addition to Mg and Si – had the lowest As concentration, likely because the only way to account for As^{5+} incorporation in the absence of paired substitution by a trivalent cation is vacancies. Serp 2 and Serp 6 represent an interesting comparison; they are both syntheses involving Mg, Si, Al, and As, where the only difference from onset of synthesis was that As^{5+} was in the Serp 2 initial solution (tubular crystals formed), compared to As^{3+} in the Serp 6 initial solution (platy

Fig. 6 Ternary diagram showing relative molar proportions of Mg, Al, and As (Table 3). Al-rich platy Mg-serpentines (Serp 4, 6) are indicated by hexagons to distinguish them from tubular serpentines.

Fig. 7 Schematic diagrams of (**a**) geometries and scaled sizes of SiO_4^{4-}, AsO_4^{3-}, AlO_4^{5-}, AsO_3^{3-}, and FeO_4^{5-} anions, arranged in order of increasing cation–O bond distance (Table 6), and (**b**) examples of substitutions of Al, Fe^{3+}, As^{5+}, and As^{3+} in tetrahedral sheets of an antigorite crystal structure (re-drawn from Capitani & Mellini 2004). The central parts of the crystals (in the broken-line box) represents a small portions of a chrysotile crystal, including an As^{3+} ion showing the problem of its pyramidal geometry (rather than tetrahedral).

crystals formed). The difference in morphology and composition implies that the oxidation state of arsenic influenced crystal nucleation and growth. Platy crystals formed when the substituted cation was Al^{3+} or Al^{3+} plus As^{3+}, but when Al^{3+} was paired with As^{5+}, tubular crystals formed. In Serp 2, the Al content apparently was too small to solve the tetrahedral-octahedral mismatch. This suggests that As^{5+} limited the incorporation of Al. Interestingly, the As content of tubular Serp 2 crystals was comparable to the other As-bearing synthesized serpentines.

For a given cation site, the most important controls on isomorphous substitution are ionic charge, crystal radius, and

Table 7 Crystal radii of pertinent cations in tetrahedral coordination as well as tetrahedral bond lengths (± 0.03 Å) for each cation

Cation	Site	Radius	Cation-O bond length
Si^{4+}	Tetrahedral	0.40 Å	1.63 Å
As^{5+}	Tetrahedral	0.48 Å	1.72 Å
Al^{3+}	Tetrahedral	0.53 Å	1.75 Å
As^{3+}	Tetrahedral	0.54 Å [a]	1.78 Å
Fe^{3+}	Tetrahedral	0.63 Å [b]	1.87 Å

Crystal radii are from Shannon (1976) except for (a) EXAFS data from Niu (2011), and (b) Meunier (2005).

The crystal radius of oxygen in tetrahedral coordination is 1.22 to 1.24 Å.

molecular geometry. Of the two As species with the potential to occur in the serpentine structure, both have charges within ± 1 of Si^{4+}. The crystal radius of As^{5+} in tetrahedral coordination (0.48 Å) is closer to that of Si (0.40 Å) than is tetrahedral Al (0.53 Å), and tetrahedral As^{3+} (0.54 Å) is nearly identical to Al. Thus, the smaller As^{5+} appears to be a better fit than As^{3+} or Al^{3+} in the tetrahedral sheet in terms of radius considerations, and XAFS data indicating the As-O bond length of 1.71 Å in Serp 5 is a very good match with theoretical As^{5+}-O distance of 1.72 Å (Table 7).

Considering valence and molecular geometry, As^{5+} readily forms tetrahedral anions with O^{2-}, e.g. AsO_4^{3-}, which can substitute for SiO_4^{4-} in the tetrahedral sheet with little special accommodation required. The difference in valence structure of AsO_4^{3-} compared to SiO_4^{4-} could be accommodated by the absence of a hydrogen atom where bonding to the octahedral sheet occurs. As^{3+}, on the other hand, tends to form AsO_3^{3-} with a pyramidal shape that effectively lacks an apical oxygen atom (Fig. 7). This geometry would probably not bond as well with the adjacent octahedral sheet as AsO_4^{3-}, although an As coordination number of 3.3 in Serp 5 (Fig. 4B, Table 5) and the XANES fit (Fig. 4A) are consistent with both As^{5+} and As^{3+} in the tetrahedral sheet (when both were included in the synthesis solution, i.e. Serp 5). From these first-principle considerations, As^{5+} is crystallographically well suited to occur in the tetrahedral sheet. As^{3+} may also occur in the tetrahedral sheet, but the pyramidal structure of AsO_3^{3-} may limit its incorporation relative to As^{5+}. XANES

analysis of Serp 5 is consistent with this, indicating that the highest oxidation state of arsenic, As^{5+}, has a greater tendency to substitute into the tetrahedral sheet than As^{3+}.
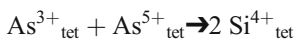
The charge imbalance of +1 that accompanies substitution of Si^{4+} by As^{5+} can be satisfied by paired substitution as follows (Hattori et al. 2005):
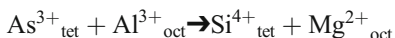
$$As^{5+}_{tet} + Al^{3+}_{tet} \rightarrow 2\ Si^{4+}_{tet}$$
$$As^{5+}_{tet} + As^{3+}_{tet} \rightarrow 2\ Si^{4+}_{tet}$$
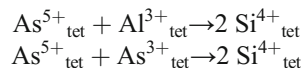
or by omission of an H^+ in the octahedral sheet, or by vacancies in the octahedral sheet, e.g.

$$2\ As^{5+}_{tet} \rightarrow 2\ Si^{4+}_{tet} + Mg^{2+}_{oct}$$
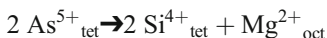
The XAS data from Niu (2011) and the present study document the occurrence of As^{3+} in the tetrahedral sheet of serpentine, and Pascua et al. (2005) identified As^{3+} in hydrothermal Mg-smectites with 1500 to 4000 mg kg^{-1} As (~0.01–0.02 As per Si_4O_{10}). The charge on As^{3+} does not limit incorporation into tetrahedral sheets, nor should size; for example, As^{3+} is smaller than the Fe^{3+} atom that occurs in tetrahedral sites of antigorite as well as other clay minerals (Wicks & O'Hanley 1988; Petit & Decarreau 1990; Petit et al. 2017). So, based on considerations of charge and radius, As^{3+} is compatible with substitution into tetrahedral sites and charge balance can be maintained as follows:

$$As^{3+}_{tet} + As^{5+}_{tet} \rightarrow 2\ Si^{4+}_{tet}$$

or:

$$As^{3+}_{tet} + Al^{3+}_{oct} \rightarrow Si^{4+}_{tet} + Mg^{2+}_{oct}$$

The latter example is similar to Tschermak substitution cited to explain the occurrence of Al in serpentine (Serna et al. 1979):

$$Al^{3+}_{tet} + Al^{3+}_{oct} \rightarrow Si^{4+}_{tet} + Mg^{2+}_{oct}$$
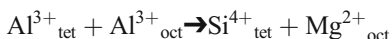
One important difference is that, unlike Si^{4+}, As^{5+}, Al^{3+}, and Fe^{3+}, which form tetrahedral anions in nature, As^{3+} does not (Fig. 7). The mostly likely orientation of the pyramidal AsO_3 in the tetrahedral sheet is one without an apical oxygen atom, leaving only an electron pair to bond with the adjacent octahedral sheet. The greater length of the As^{3+}–O bond compared to the Si–O bond – plus the lack of an apical O atom (Fig. 7) – indicates that As^{3+} will have a tendency to distort the crystal structure in order to fit, so it may occupy tetrahedral sites at edges where size and bonding is less of a constraint. In antigorite, relatively large cations occur where tetrahedral sheets undergo inversion to satisfy the octahedral-tetrahedral mismatch (Moore & Reynolds 1997). The thicknesses (*c*-axis dimension) of the largest tetrahedral sites in antigorite (at inversions; Fig. 7) are 0.10–0.15 Å greater than non-inversion sites and tetrahedral bond lengths are commensurately greater at inversion sites (Capitani & Mellini 2004). This implies that the stability of the antigorite structure would be less impacted if As^{3+} (or Al^{3+}, As^{5+}, or Fe^{3+}) were to occupy the larger tetrahedral inversion sites. The tubular structure of chrysotile involves distortions in the tetrahedral sheet that may accommodate As^{3+}, and the often-high levels of Al in lizardite imply the potential to incorporate As^{3+}.

The heterogeneity in As concentration in these synthesized serpentines (TEM-AEM data) and in naturally occurring antigorites implies that the incorporation of As into serpentine is kinetically controlled and dictated by solution composition. The synthesized serpentine crystals contained As concentrations ranging from < 1 mg kg^{-1} to 20,000 mg kg^{-1} (equivalent to as high as 0.2 mol As per 2 mol tetrahedral sites) and EMPA shows that As in natural antigorite can range from < 100 mg kg^{-1} to 1300 mg kg^{-1} over a scale of ~100 µm (Niu 2011). The heterogeneity indicates that As content in antigorite is related to local-scale differences in As availability during antigorite crystallization, consistent with influence of kinetic control on the variable levels of As incorporation into serpentine. It may also be a consequence of rapid crystallization. Compositional heterogeneity extends to Al and Fe in natural serpentines as well, as Yariv & Heller-Kallai (1975) documented, by EMPA analysis, extensive variability in isomorphous substitutions of Al that led them to state "some serpentines are so inhomogeneous that it is questionable whether the average chemical composition has any real significance." Given these observations, two questions that this current study does not directly address are the effect of Fe on incorporation of As into Mg clays, and whether or not longer reaction time during synthesis would produce more homogeneous crystal compositions.

As-bearing Trioctahedral Clay Minerals in the Context of the Arsenic Cycle

Serpentinization of ultramafic rocks and crystallization of smectite in an intermediate-to-alkaline hydrothermal system are the two known environments that foster incorporation of arsenic into tetrahedral sites in Mg-phyllosilicates (Fig. 8). Evidence for this particular speciation includes XANES and XAFS analyses of antigorite, chlorite, and synthesized serpentine, indicating that both As^{5+} and As^{3+} occur in tetrahedral sites (Hattori et al. 2005; Ryan et al. 2011; Masuda et al. 2012). The EMPA and TEM analysis of natural antigorites, chlorites, and Mg-smectites indicate As concentrations that attain ~10^3 ppm (0.1 wt.%, 0.01 to 0.02 mol per Si_2O_5 or Si_4O_{10} unit cell), and compositions of synthesized serpentines indicate the potential to reach the order of 10^4 ppm As (1 wt.%, 0.1–0.2 As per 2 tetrahedral sites). Sequential chemical extraction and EMPA of talc is consistent with the occurrence of As at concentrations of 65 to 80 mg kg^{-1}, presumably in tetrahedral sites (Ryan et al. 2011; Boskabadi et al. 2017).

In high-temperature systems, As is transported with other fluid-mobile elements (e.g. B, Sb, Cs) in waters derived from subducting sediments (Fig. 8), and the fate of As in these waters is controlled to some extent by Mg-rich clay minerals. If the waters react with upper-mantle rock, they may form serpentine or chlorite that fixes As, providing insight into processes associated with subduction, serpentinization, and subsequent metamorphism (Hattori et al. 2005; Deschamps et al. 2010). If the waters evolve into shallow alkaline
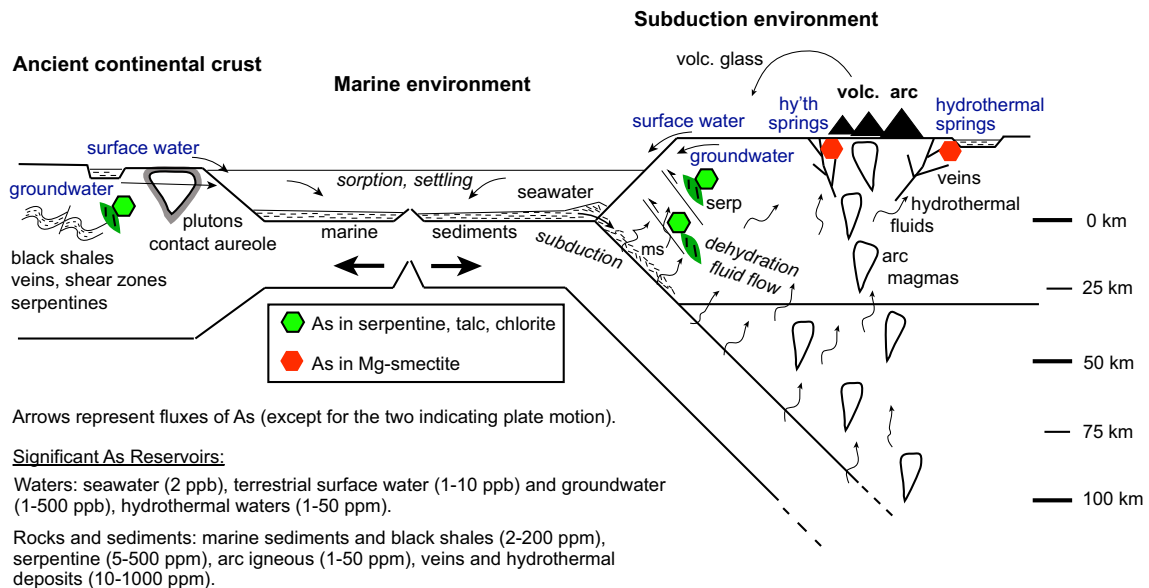
Fig. 8 Schematic illustration of the arsenic cycle, emphasizing occurrence of trioctahedral Mg silicates (hexagonal symbols). Concentrations in most reservoirs are quite variable, so the values shown at the lower left, with one exception (seawater), attempt to represent this variability. The symbol "ms" indicates metasedimentary rock. Sources for As reservoir concentrations are Smedley & Kinniburgh (2002), Milham & Craw (2009), Ryan et al. (2011), and Breuer & Pichler (2013). Diagram adapted from Deschamps et al. (2010) and Masuda (2018).

hydrothermal systems, As may become fixed into tetrahedral sheets when Mg-smectite crystallizes (Pascua et al. 2005). While shallow hydrothermal systems are recognized as a source of elevated As in groundwater, more research is needed to ascertain the role that As-bearing clays might exert in controlling As fate and transport in these systems (López et al. 2012).

Given the association of Mg clays with alkaline environments of formation, including serpentinizing fluids and intermediate-to-alkaline hydrothermal systems (Inoue 1995; Lafay et al. 2016), and the occurrence of the AsO_4^{3-} oxyanion in alkaline waters, it is likely that the optimal conditions for fixing As into clay-mineral tetrahedral sites occurs when clays precipitate from alkaline fluids. Conditions like these occur in near-surface hydrothermal (~100°C; Pascua et al. 2005) and deeper lithosphere serpentinizing systems (~250°C; Deschamps et al. 2010), and perhaps in alkaline surface waters where Mg-smectite, kerolite, sepiolite, and associated Mg clays crystallize (Jones & Conko 2011).

In earth surface hydrologic systems, As in tetrahedral sites of antigorite and chlorite has been identified as a source of elevated As in groundwater, emphasizing the importance of understanding this particular speciation. Trioctahedral clay minerals may function either as a direct source of As to aquifers by way of in situ chemical weathering (Ryan et al. 2011; Masuda et al., 2012) or by weathering in a sedimentary source area where As becomes fixed into secondary minerals (e.g. Fe (oxyhydr)oxides) that are then transported into the aquifer (Hattori et al. 2005; Guillot & Charlet 2007). In both scenarios, understanding of the role of silicate clays as a

potential As source is needed for accurate models (Mukherjee et al. 2014; Masuda 2018).

Incorporation of As depends on many environmental factors, including fluid composition, reduction-oxidation potential (as fO_2, Eh or pe; Fig. 9), pH, temperature, co-precipitation, and likely microbial influences (depending on setting). The concentration of As in hydrothermal waters ranges generally from <1 to 50 mg/L (Ballantyne & Moore 1988; Webster &
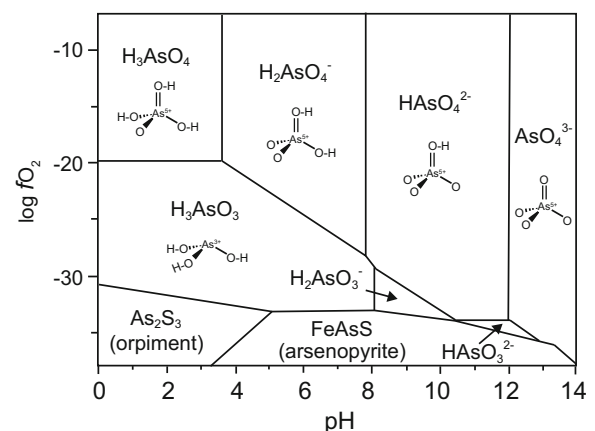
Fig. 9 fO_2-pH diagram for a fluid system at 250°C showing speciation of arsenic as a function of pH and redox conditions, where oxygen fugacity (fO_2) is a measure of oxidation-reduction potential of mineralizing fluids (higher values indicating more oxidizing). This system includes As, S, Fe, and O, and indicates the propensity for As to occur as tetrahedral anions at moderate to high oxygen fugacity across a wide range of pH. Modified from James-Smith et al. (2010).

Nordstrom 2003), making the As concentrations in the synthesis solutions an apt comparison (16.7 or 33.3 mg/L As; Table 2). While it is not possible to measure concentrations of fluids deep in suprasubduction zones, evidence from shallower systems suggests that As concentrations may range from <10 to 10^2 or 10^3 mg/L (Breuer & Pichler 2013). Thus, the incorporation of As into up to 10% of tetrahedral sites of Mg phyllosilicates synthesized in the current study, i.e. when [As] in solution is on the order of 10^1 to 10^2 mg/L, provides a reference point for natural systems.

Aqueous As^{5+} species are stable over a wide range of redox conditions, pH, and temperature (Shock et al. 1997), and the suprasubduction zone fluids that foster serpentinization of peridotites evolve towards alkaline solutions with pH $\geq$ 10 (e.g. Barnes & O'Neil 1969), conditions where tetrahedral AsO_4^{3-} would be available for incorporation in serpentine group minerals. In neutral to acidic systems, protonation of AsO_4^{3-} to $HAsO_4^{2-}$, $H_2AsO_4^-$, and H_3AsO_4 could limit incorporation into the tetrahedral sheet. In reducing conditions and with decreasing pH, reduction of As^{5+} to As^{3+} and eventually As^{3-} or As^0 would preclude fixation into the silicate structure, and instead fix As into arsenides or sulfides (Fig. 9; Ishimaru & Arai 2008; Deschamps et al. 2010). Redox conditions that favor the presence of As^{3+} in mineralizing solutions may result in serpentines with no As^{5+} and relatively large amounts of As^{3+}, and if Eh conditions are low-intermediate, a mix of As^{5+} and As^{3+} may occur in the same crystal; in this way, As oxidation state may record redox conditions of lithospheric waters (Hattori et al. 2005).

CONCLUSIONS

Tubular and platy arsenic-bearing serpentines were synthesized at 200°C in alkaline solutions for reactions of 10 days' duration. The arsenic occurs as As^{5+}, As^{3+}, or both, in tetrahedral sites of serpentine at levels reaching 10^4 mg kg^{-1} (ppm); future analyses using Al NMR and Si EXAFS would help to corroborate these results. The tetrahedral AsO_4^{3-} oxyanion appears to be particularly well suited for substitution into the tetrahedral sheet, and alkaline conditions that favor crystallization of Mg clays coincide with As occurrence as AsO_4^{3-} (or in reduced waters, AsO_3^{3-}). This explains the occurrence of tetrahedral As in serpentine-group minerals, chlorite, Mg-smectites, and talc, and suggests that As may also occur in other Mg clays that form in alkaline environments, e.g. sepiolite and palygorskite.

ACKNOWLEDGMENTS

Compliance with Ethical Standards

Conflict of Interest

REFERENCES

Arai, Y., Elzinga, E. J., & Sparks, D. L. (2001). X-ray absorption spectroscopic investigation of arsenite and arsenate adsorption at the aluminum oxide–water interface. *Journal of Colloid and Interface Science, 235*, 80–88.

Ballantyne, M., & Moore, J. N. (1988). Arsenic geochemistry in geothermal systems. *Geochimica et Cosmochimica Acta, 52*, 475–483.

Barnes, I., & O'Neil, J. R. (1969). The relationship between fluids in some fresh alpine type ultramafics and possible modern serpentinization, western United States. *Geological Society of America Bulletin, 80*, 1947–1960.

Bentabol, M., Ruiz Cruz, M. D., Huertas, F. J., & Linares, J. (2006). Hydrothermal synthesis of Mg- and Mg-Ni-rich kaolinite. *Clays and Clay Minerals, 54*, 667–677.

Bentabol, M., Ruiz Cruz, M. D., & Huertas, F. J. (2007). Synthesis of Ni-rich 1:1 phyllosilicates. *Clays and Clay Minerals, 55*, 572–582.

Bentabol, M., Ruiz Cruz, M. D., & Huertas, F. J. (2009). Hydrothermal synthesis (200°C) of Co–kaolinite and Al–Co–serpentine. *Applied Clay Science, 42*, 649–656.

Bentabol, M., Ruiz Cruz, M., & Sobrados, I. (2010). Chemistry, morphology and structural characteristics of synthetic Al-lizardite. *Clay Minerals, 45*, 131–143.

Bhattacharya, P., Welch, A. H., Stollenwerk, K. G., McLaughlin, M., Bundschuh, J., & Panaullah, G. (2007). Arsenic in the environment: biology and chemistry. *Science of the Total Environment, 379*, 109–120.

Boskabadi, A., Pitcairn, I. K., Broman, C., Boyce, A., Teagle, D. A. H., Cooper, M. J., Azer, M. K., Stern, R. J., Mohamed, F. H., & Majka, J. (2017). Carbonate alteration of ophiolitic rocks in the Arabian–Nubian Shield of Egypt: sources and compositions of the carbonating fluid and implications for the formation of Au deposits. *International Geology Review, 59*, 391–419.

Breuer, C., & Pichler, T. (2013). Arsenic in marine hydrothermal fluids. *Chemical Geology, 348*, 2–14.

Brindley, G. W., & Brown, G. (1980). *Crystal Structures of Clay Minerals and their X-ray Identification*. Monograph 5, Mineralogical Society, London.

Capitani, G., & Mellini, M. (2004). The modulated crystal structure of antigorite: The m=17 polysome. *American Mineralogist, 89*, 147–158.

Čavajda, V., Uhlík, P., Derkowski, A., Čaplovičová, M., Madejová, J., Mikula, M., & Ifka, T. (2015). Influence of grinding and sonication on the crystal structure of talc. *Clays and Clay Minerals, 63*, 311–327.

Charnock, J. M., Polya, D. A., Gault, G., & Wogelius, R. (2007). Direct EXAFS evidence for incorporation of As^{5+} in the tetrahedral site of natural andraditic garnet. *American Mineralogist, 92*, 1856–1861.

Chukanov, N. V. (2014). *Infrared Spectra of Mineral Species: Extended Library, volume 1*. Berlin: Springer.

Cliff, G., & Lorimer, G. W. (1975). The quantitative analysis of thin specimens. *Journal of Microscopy, 103*, 203–207.

Craw, D., Landis, C. A., & Kelsey, P. I. (1987). Authigenic chrysotile formation in the matrix of Quaternary debris flows, northern Southland, New Zealand. *Clays and Clay Minerals, 35*, 43–52.

Deer, W. A., Howie, R. A., & Zussman, J. (2009). *Rock-Forming Minerals vol. 3B, Layered Silicates Excluding Micas and Clay Minerals. 2nd edition*. London: Geological Society.

Deschamps, F., Guillot, S., Godard, M., Chauvel, C., Andreani, M., & Hattori, K. (2010). In situ characterization of serpentinites from forearc mantle wedges: timing of serpentinization and behavior of fluid-mobile elements in subduction zones. *Chemical Geology, 269*, 262–277.

Dódony, I., Pósfai, M., & Buseck, P. R. (2002). Revised structure models for antigorite: An HRTEM study. *American Mineralogist, 87*, 1443–1457.

Farmer, V. C. (1974). The layer silicates. In V. C. Farmer (Ed.), *The Infrared Spectra of Minerals* (pp. 331–365). London: Mineralogical Society.

Farmer, V. C., & Russell, J. D. (1967). Infrared absorption spectrometry in clay studies. *Clays and Clay Minerals, 15*, 121–142.

Frost, R. L., Xi, Y., Pogson, R. E., & Scholz, R. (2013). A vibrational spectroscopic study of philipsbornite PbAl$_3$(AsO$_4$)(OH)$_5$·H$_2$Omolecular structural implications and relationship to the crandallite subgroup arsenates. *Spectrochimica Acta Part A: Molecular and Biomolecular Spectroscopy, 104*, 257–261.

Fuchs, Y., Linares, J., & Mellini, M. (1998). Mössbauer and infrared spectrometry of lizardite-1T from Monte Fico, Elba. *Physics and Chemistry of Minerals, 26*, 111–115.

Guillot, S., & Charlet, L. (2007). Bengal arsenic, an archive of Himalaya orogeny and paleohydrology. *Journal of Environmental Science and Health A, 42*, 1785–1794.

Hattori, K., Takahashi, Y., Guillot, S., & Johanson, B. (2005). Occurrence of arsenic (V) in forearc mantle serpentinites based on X-ray absorption spectroscopy study. *Geochimica et Cosmochimica Acta, 69*, 5585–5596.

Inoue, A. (1995). Formation of clay minerals in hydrothermal environments. In B. Velde (Ed.), *Origin and Mineralogy of Clays* (pp. 268–329). Berlin: Springer.

Iriarte, I., Petit, S., Huertas, F. J., Fiore, S., Grauby, O., Decarreau, A., & Linares, J. (2005). Synthesis of kaolinite with a high level of Fe^{3+} for Al substitution. *Clays and Clay Minerals, 53*, 1–10.

Ishimaru, S., & Arai, S. (2008). Arsenide in a metasomatized peridotite xenolith as a constraint on arsenic behavior in the mantle wedge. *American Mineralogist, 93*, 1061–1065.

James-Smith, J., Cauzid, J., Testamale, D., Liu, W., Hazemann, J.-L., Proux, O., Etschmann, B., Philipott, P., Banks, D., Williams, P., & Brugger, J. (2010). Arsenic speciation in fluid inclusions using micro-beam X-ray absorption spectroscopy. *American Mineralogist, 95*, 921–932.

Jones, B. F., & Conko, K. M. (2011). Environmental influences on the occurrences of sepiolite and palygorskite: A brief review. *Developments in Clay Science, 3*, 69–83.

Lafay, R., Montes-Hernandez, G., Janots, E., Munoz, M., Auzende, A. L., Gehin, A., Chiriac, R., & Proux, O. (2016). Experimental investigation of As, Sb and Cs behavior during olivine serpentinization in hydrothermal alkaline systems. *Geochimica et Cosmochimica Acta, 179*, 177–202.

Liu, S., Jing, C., & Meng, X. (2008). Arsenic re-mobilization in water treatment adsorbents under reducing conditions: Part II. *XAS and modeling study. Science of The Total Environment, 392*, 137–144.

López, D. L., Birkle, P., Bundschuh, J., Sracek, O., Armienta, M. A., Cornejo, L., & Ormachea, M. (2012). Arsenic in geothermal waters of volcanic–magmatic systems of Latin America. *Science of the Total Environment, 429*, 57–75.

Masuda, H. (2018). Arsenic cycling in the Earth's crust and hydrosphere: interaction between naturally occurring arsenic and human activities. *Progress in Earth and Planetary Science, 5*, 68.

Masuda, H., Shinoda, K., Okudaira, T., Takahashi, Y., & Noguchi, N. (2012). Chlorite – source of arsenic groundwater pollution in the Holocene aquifer of Bangladesh. *Geochemical Journal, 46*, 381–391.

Mellini, M., Fuchs, Y., Viti, C., Lemaire, C., & Linares, J. (2002). Insights into the antigorite structure from Mössbauer and FTIR spectroscopies. *European Journal of Mineralogy, 14*, 97–104.

Méring, J. (1949). L'intereférence des Rayons X dans les systèmes à stratification désordonée. *Acta. Crystallographica, 2*, 371–377.

Meunier, A. (2005). *Clays*. Berlin: Springer-Verlag.

Milham, L., & Craw, D. (2009). Two-stage structural development of a Paleozoic auriferous shear zone at the Globe-Progress deposit, Reefton, New Zealand. *New Zealand Journal of Geology and Geophysics, 52*, 247–259.

Moore, D. M., & Reynolds Jr., R. C. (1997). *X-ray Diffraction and the Identification and Analysis of Clay Minerals*. New York: Oxford University Press.

Mukherjee, A., Verma, S., Gupta, S., Henke, K., & Bhattacharya, P. (2014). Influence of tectonics, sedimentation and aqueous flow cycles on the origin of global groundwater arsenic: paradigms from three continents. *Journal of Hydrology, 518*, 284–299.

Müller, K., Ciminelli, V. S. T., Dantas, M. S. S., & Willscher, S. (2010). A comparative study of As(III) and As(V) in aqueous solutions and adsorbed on iron oxy-hydroxides by Raman spectroscopy. *Water Research, 44*, 5660–5672.

Myneni, S. C. B., Traina, S. J., Waychunas, G. A., & Logan, T. J. (1998). Experimental and theoretical vibrational spectroscopic evaluation of arsenate coordination in aqueous solutions, solids, and at mineral-water interfaces. *Geochimica et Cosmochimica Acta, 62*, 3285–3300.

Navas-Acien, A., Silbergeld, E. K., Pastor-Barriuso, R., & Guallar, E. (2010). Arsenic exposure and prevalence of type 2 Diabetes in US adults. *Journal of the American Medical Association, 300*, 814–822.

Newville, M. (2001). IFEFFIT: interactive XAFS analysis and FEFF fitting. *Journal of Synchrotron Radiation, 8*, 322–324.

Niu, L. (2011). Arsenic distribution and speciation in antigorite-rich rocks from Vermont, USA. M.Sc. thesis, Univ. Ottawa, Ontario, Canada, 111 pp.

Opiso, E. M., Sato, T., Morimoto, K., Asai, A., Anraku, S., Numako, C., & Yoneda, T. (2010). Incorporation of arsenic during the formation of Mg-bearing minerals at alkaline condition. *Minerals Engineering, 23*, 230–237.

Pascua, C., Charnock, J., Polya, D. A., Sato, T., Yokoyama, S., & Minato, M. (2005). Arsenic bearing smectite from the geothermal environment. *Mineralogical Magazine, 69*, 897–906.

Petit, S., & Decarreau, A. (1990). Hydrothermal (200°C) synthesis and crystal chemistry of iron-rich kaolinites. *Clay Minerals, 25*, 181–196.

Petit, S., Baron, F., & Decarreau, A. (2017). Synthesis of nontronite and other Fe-rich smectites: a critical review. *Clay Minerals, 52*, 469–483.

Ravel, B., & Newville, M. (2005). ATHENA, ARTEMIS, HEPHAESTUS: data analysis for X-ray absorption spectroscopy using IFEFFIT. *Journal of Synchrotron Radiation, 12*, 537–541.

Rehr, J. J., Kas, J. J., Vila, F. D., Prange, M. P., & Jorissen, K. (2010). Parameter-free calculations of X-ray spectra with FEFF9. *Physical Chemistry and Chemical Physics, 12*, 5503–5513.

Rozalén, M., Ramos, M. E., Fiore, S., Gervilla, F., & Huertas, F. J. (2014). Effect of oxalate and pH on chrysotile dissolution at 25 °C: An experimental study. *American Mineralogist, 99*, 589–600.

Ryan, P. C., Kim, J., Wall, A. J., Moen, J. C., Corenthal, L. G., Chow, D. R., Sullivan, C. M., & Bright, K. S. (2011). Ultramafic-derived arsenic in a fractured bedrock aquifer. *Applied Geochemistry, 26*, 444–457.

Serna, C. J., White, J. L., & Velde, B. D. (1979). The effect of aluminium on the infra-red spectra of 7 Å trioctahedral minerals. *Mineralogical Magazine, 43*, 141–148.

Shannon, R. D. (1976). Revised effective ionic radii and systematic studies of interatomic distances in halides and chalcogenides. *Acta Crystallografica, A32*, 751–767.

Shi, X., Ayotte, J. D., Onda, A., Miller, S., Rees, J., Gilbert-Diamond, D., Onega, T., Gui, J., Karagas, M., & Moeschler, J. (2015). Geospatial association between adverse birth outcomes and arsenic

in groundwater in New Hampshire, USA. *Environmental Geochemistry and Health, 37*, 333–351.

Shock, E. L., Sassani, D. C., Willis, M., & Sverjensky, D. A. (1997). Inorganic species in geologic fluids: Correlations among standard molal thermodynamic properties of aqueous ions and hydroxide complexes. *Geochimica et Cosmochimica Acta, 61*, 907–950.

Smedley, P. L., & Kinniburgh, D. G. (2002). A review of the source, behavior and distribution of As in natural waters. *Applied Geochemistry, 17*, 517–568.

Suquet, H. (1987). Effects of dry grinding and leaching on the crystal structure of chrysotile. *Clays and Clay Minerals, 37*, 439–445.

Takahashi, Y., Ohtaku, N., Mitsunobu, S., Yuita, K., & Nomura, M. (2003). Determination of the As(III)/As(V) Ratio in Soil by X-ray Absorption Near-edge Structure (XANES) and Its Application to the Arsenic Distribution between Soil and Water. *Analytical Sciences, 19*, 891–896.

Viti, C., & Mellini, M. (1997). Contrasting chemical compositions in associated lizardite and chrysotile in veins from Elba, Italy. *European Journal of Mineralogy, 9*, 585–596.

Webster, J. G., & Nordstrom, D. K. (2003). Geothermal arsenic: the source, transport and fate of arsenic in geothermal systems. In A. H. Welch & K. G. Stollenwerk (Eds.), *Arsenic in Ground Water: Geochemistry and Occurrence* (pp. 101–126). New York: Kluwer Academic Publishers.

Wicks, F. F., & O'Hanley, D. S. (1988). Serpentine minerals: structures and properties. In S. W. Bailey (Ed.), *Hydrous Phyllosilicates, Reviews in Mineralogy 19* (pp. 91–167). Washington, D.C.: Mineralogical Society of America.

Yariv, S., & Heller-Kallai, L. (1975). The relationship between the IR spectra of serpentines and their structures. *Clays and Clay Minerals, 23*, 145–152.